Global Surface Soil Moisture Drydown Patterns

Vinit Sehgal[1], Nandita Gaur[2,3], Binayak P. Mohanty[3]

[1]Water Management and Hydrological Science, Texas A& M University, TX 77840, USA
[2]Department of Crop and Soil Sciences, University of Georgia, Athens, GA 30602, USA.
[3]Biological and Agricultural Engineering, Texas A&M University, TX 77840, USA.

Key Points:

- Quantification of global soil moisture drydown patterns at SMAP footprints using a non-parametric method
- Seasonally variable soil, vegetative and atmospheric controls are observed in effective soil water retention parameters at SMAP footprint
- Inter-seasonal variability in soil drydown parameters is governed by climate and landuse.

Corresponding author: Binayak P. Mohanty, bmohanty@tamu.edu

Abstract

Understanding the global soil moisture (SM) dynamics and its governing controls beyond Darcy Scale is critical for various hydrologic, meteorological, agricultural, and environmental applications. In this study, we parameterize the pathways of the seasonal drydowns using global surface soil moisture (θ_{RS}) observation from SMAP satellite (between 2015 and 2019) at 36km X 36km. We develop a new data-driven non-parametric approach to identify the canonical shapes of θ_{RS} drydown, followed by a non-linear least-squares parameterization of the seasonal drydown pathways at each SMAP footprint. The derived parameters provide the effective soil water retention parameters (SWRP_{eff}), land-atmospheric coupling strength, soil hydrologic regimes for SMAP footprint. Depending on footprint heterogeneity, climate and season, the characteristics curves comprising different drydown phases are discovered at SMAP footprints. Drydown curves respond to the within-footprint changes in the meteorological drivers, land-surface characteristics and the soil-vegetative and atmospheric dynamics. Drydown parameters display high inter-seasonal variability, especially in grasslands, croplands and savannah landscapes due to significant changes in the landscape characteristics and moisture patterns at the subgrid-scale. Soil texture exert influence on the characteristics soil water retention and drydown parameters only when the footprint mean θ_{RS} is low, specifically in arid and sparsely vegetated regions. The influence of soil texture on the inter-seasonal variability of SWRP_{eff} is low compared to landuse and climate at RS-footprint scale. The global understanding of characteristics SM drydown features at SMAP footprints provides a significant step towards a scale-specific, effective soil hydrologic parameterization for various applications.

1 Introduction

Soil moisture (SM) accounts for a small fraction of the total global freshwater, yet exerts a large influence on the global water cycle (McColl, Alemohammad, et al., 2017) At fine scale, soil governs plant growth, geo-chemical processes and groundwater recharge. However at large spatial scales (several hundred meters to several kms), SM plays a crucial role in precipitation recycling (Baudena et al., 2008), cloud formation (Fast et al., 2019), land-atmospheric coupling (Schwingshackl et al., 2018) and numerous other critical processes for global energy, water and carbon cycle. Global SM status and the characteristic soil water retention functions are needed as inputs to the large-scale Earth-system-modeling (Bonan & Doney, 2018; Dunne et al., 2012; Flato, 2011; Hurrell et al., 2013). However, the mechanistic understanding (and modeling) of SM dynamics for large-spatial scales is yet mainly driven by a Darcy-scale perspective, largely due to the unavailability of large-scale historic observed data until very recently. Hence, there is a need to critically re-evaluate the processes and to develop new understandings/ interpretations about the governing processes of SM, specific to large spatial scales.

The general trajectory of SM drydowns (period of sustained loss of SM) finds its origin from fine-scale studies (Guswa et al., 2002; Rodriguez-Iturbe, 2000; Rodriguez-Iturbe et al., 1999). Laio et al. (2001) proposed that mapping the trajectory of the rate of loss of SM with decreasing SM can provide information about the dominant soil hydrologic regimes and the soil water retention properties like field capacity and wilting point. The pathway of SM drydown was assumed to be a piecewise-linear function where each limb represented a unique soil hydrologic regime. Moreover, the rate of drainage loss and land-atmospheric interactions may also be inferred from the SM drydown curves. Operating in the L-band microwave frequency, SMAP radiometer provides SM estimates for the top 5-cm of soil with a high retrieval accuracy at a spatial support scale of 36 km. The spatial support (36 km) and global extent make SMAP observations ideal for a global evaluation of SM drydowns at large spatial scales.

However, unlike fine scale, where SM drydown is governed by soil properties, SM drydown at the remote sensing (RS)- footprint scale represents the effective manifestation of the subgrid-scale variability in the soil hydraulic (texture and structure), vegetation (root-water uptake, transpiration) characteristics, and overall atmospheric conditions (Crow et al., 2012; Gaur & Mohanty, 2013, 2016, 2019; Vivoni et al., 2010). At large spatial scales, the coupled soil-vegetation-climate (SVC) dynamics can influence the patterns of SM drydown (D'Odorico et al., 2000; Laio et al., 2001; Rodriguez-Iturbe et al., 1999). Gaur and Mohanty (2019) showed that SM drydowns at these scales can be modeled as quantitative functions of subgrid-scale land surface heterogeneity (soil, vegetation and topography) depending on the hydro-climate. Several other studies have also shown that the effective SM dynamics at RS-footprint scales are moderated by subgrid-scale variability in the soil and land-surface characteristics like soil texture, soil composition, topography and slope (Gaur & Mohanty, 2013, 2016), vegetation characteristics (pattern, type and growth) (Ivanov et al., 2010), spatial distribution of precipitation and drainage patterns etc. (Kathuria et al., 2019).

The effective control of the SVC dynamics and subgrid-scale land-surface characteristics on SM drydown also show significant inter-seasonal variability (Viola et al., 2008). For example, lack of moisture may impede vegetation growth and the spatial variability in the SM distribution may reduce significantly during dry seasons, effectively decreasing the sub-grid scale SM variability. Similar effect is observed during wet conditions as excess moisture reduces the subgrid-scale SM variability, especially in sparsely vegetated regions. Precipitation intensity, duration and patterns may change significantly over seasons leading to differential flows, drainage and infiltration patterns, leading to a non-unique relationship between the effective value of the observed SM and the effective SM drying rate for the pixel. Hence, the effective SM drydown at RS footprint scale can be best assumed to be multi-dimensional process with a dynamic dependency on both atmospheric forcings and subgrid-scale SM variability in the footprint. Hence, including a seasonal "dimension" in the SM drydown can help capture the combined variability in the SVC dynamics and the land-surface heterogeneity and SM variability, reduce uncertainty in estimating the pathways and parameters of SM drydown, and identify the spatial and temporal evolution of the governing controls of SM dynamics at RS footprint scale. Recently, Haghighi et al. (2018) demonstrated the time-varying dependencies of Evaporative Fraction (EF)-SM relationship with changing atmospheric drivers using ground-based observations. However, the influence of the seasonally varying atmospheric drivers and changing land-surface heterogeneity on θ_{RS} drydown at RS-footprint scale largely remains a topic of active research.

The objective of this study is to develop a quantified understanding of the global SM dynamics through derivation of the seasonal soil water retention and drydown parameters (SWRP_{eff}) using footprint-scale SM time series dataset of SMAP. We parameterize the pathways of SM drydown at RS-footprint scale using an unsupervised, data-driven approach. A new non-parametric approach is developed to first identify the functional forms of θ_{RS} drydown at RS footprint scale. The spatial and seasonal variability in the drydown pathways and parameters is studied w.r.t changing soil, vegetation and atmospheric (climatic) conditions at a seasonal time-scale. The study discusses the application of the θ_{RS} drydown parameters in understanding land-atmosphere coupling, estimate pixel-scale SWRP_{eff} and identify the dominant soil hydrologic regimes at a global scale.

2 Dataset

2.1 Remotely sensed SM observations from SMAP

Global surface SM observations (θ_{RS}) for the period of analysis are obtained from Soil Moisture Active Passive (SMAP) for a period of 31^{st} March 2015 to 19^{th} March 2019. SMAP uses L-band microwave radiometer at 1.41 GHz to retrieve global surface (0-5 cm) SM with

2-3 days revisit at the radiometer footprint of 40 km) gridded at 36 km (nested) Equal-Area Scalable Earth grid version-2 (Jackson et al., 2018; ONeill et al., 2010). Explicit considerations to mitigate the radio frequency interference provide significant improvement in the retrieval accuracy of brightness temperature from the earth's surface compared to its predecessor SM measuring missions (Colliander et al., 2017). Quality-flagged data is omitted from the analysis, which includes pixels with high water fraction (>1%), high radio frequency interference and vegetation water content (VWC), snow cover, flooding, large and highly variable slopes, or urban areas. A threshold of VWC i.e., 7 kg/m^2 is used to flag (and filter out) SMAP observation. Selective filtering of θ_{RS} based on VWC excludes pixels primarily from deciduous, evergreen and mixed forests (Chan et al., 2013) and increases the spatial coverage of SMAP over croplands and grasslands, while not drastically compromising on retrieval accuracy (Akbar et al., 2018). Both descending (6 A.M.) and ascending overpass (6 P.M.) retrievals are considered within the mission accuracy target of 0.04 cm^3/cm^3 unbiased root mean squared error for unfrozen land surfaces (without snow/ice and dense vegetation) with the improved land surface temperature correction approach implemented in the latest version of SMAP algorithm (Jackson et al., 2018). Hence, both ascending and descending overpass retrievals are used in this study, which provides a higher temporal sampling frequency. To mitigate the influence of diurnal variability in SM, the quality-screened SMAP observations are interpolated linearly to a uniform sampling frequency of 2-days at 6 A.M. local time. Hyper-arid regions (see next subsection) like the Arabian peninsula and Sahara desert are not considered in this study due to very small dynamic range, high noise and dry-bias in SMAP retrievals (Burgin et al., 2017; Kolassa et al., 2018; Reichle et al., 2015).

2.2 Ancillary dataset

We use Aridity Index (AI) as a generalized climate classification for the study. AI is calculated as a ratio of the mean annual precipitation to the mean annual reference evapotranspiration. Global estimates of AI are obtained from the Global Aridity Index and Potential Evapotranspiration ($ET_\circ$) Climate Database (version 2) which is based on global climate records from 1970 through 2000 (Fick & Hijmans, 2017; Trabucco & Zomer, 2019). Based on the aridity classification by the United Nations Environment Programme (UNEP (1997)), the global landmass is classified in five categories namely, *i*) hyper-arid, *ii*) arid, *iii*) semi-arid, *iv*) dry sub-humid and *v*) humid. Dominant landcover for each pixel is based on the classification by the International Geosphere-Biosphere Programme (IGBP, Belward et al. (1999)). The information on percent clay (%clay) at a global scale is obtained from the Harmonized World Soil Database (version 1.2) i.e. HWSD-v1.2 (Nachtergaele et al., 2012). All gridded ancillary dataset used in this study is aggregated (upscaled) to match the SMAP pixel resolution prior to the analysis.

3 Methodology

At large spatial scales, the net lateral fluxes in the soil profile of uniform depth (5 cm for SMAP) can be assumed to be negligible (Das, et al., 2008; Zhu Mohanty, 2002). Hence, any loss in the SM after precipitation, can be affiliated to infiltration (I), evapotranspiration (ET), and drainage (D). The rate of loss of SM (ET+D+I) between time t and t-1 is given by $[-\Delta\theta_{RS}/\Delta t]$, where $-\Delta\theta_{RS} = {\theta_{RS}}^{t} - {\theta_{RS}}^{t-1}$ (negative sign indicates net loss in SM). The functional relationship between $[\theta_{RS}]$ v/s $[-\Delta\theta_{RS}/\Delta t]$ is called the SM drydown function i.e. $\boldsymbol{L(\theta_{RS})}$. We assume that the SM drydowns can be represented in the form of a piecewise-linear function. A two-step approach is used for an unsupervised, data-driven estimation of the shape and parameters of $\boldsymbol{L(\theta_{RS})}$. In Step 1, globally dominant canonical shapes of θ_{RS} drydown are identified using a new non-parametric approach. The globally dominant canonical shapes from Step 1 form the basis of a (Step 2) nonlinear least-squares parametric fitting (with cross validation and resampling) to estimate the parameters and constituent regimes of $\boldsymbol{L(\theta_{RS})}$. This two-step approach ensures an unbiased estimation of the shape

and the parameters of $\boldsymbol{L(\theta_{RS})}$. Observations where $[-\Delta\theta_{RS}/\Delta t]$ <1% of the range of θ_{RS} are ignored to *i*) account for the retrieval noise in SMAP data and, *ii*) avoid conditions where several consecutively flagged or missed SMAP retrievals may cause $|\Delta t| >> |\Delta\theta_{RS}|$, leading to anomalously small values of $[-\Delta\theta_{RS}/\Delta t]$.

3.1 Step 1: Non-parametric canonical shapes of $\boldsymbol{L(\theta_{RS})}$

We express the trajectory of rate of θ_{RS} loss with decreasing θ_{RS} using a ternary combination of three distinct phases, namely, *i*) falling-rate loss (F), where mean $[-\Delta\theta_{RS}/\Delta t]$ decreases with decreasing θ_{RS}, *ii*) constant-rate loss (C) i.e. soil dries at a near-constant rate *iii*) rising-rate loss (R) where $[-\Delta\theta_{RS}/\Delta t]$ increases as soil dries. If the observed range of SM is divided into n partitions, then by comparing the mean $[-\Delta\theta_{RS}/\Delta t]$ within each subsequent (drier) partition, a trajectory of the SM drydown from wetter to dryer conditions can be indicated in terms of F, C and/or R-rate of SM loss. For (n) number of partitions over the dynamic range of θ_{RS}, $\boldsymbol{L}(\theta_{RS})$ may follow a canonical form out of the 3^{n-1} possible combinations of F, C and/or R. Inclusion of all three scenarios (C-, F- and R-rate) ensures that the non-parametric approach is non-assumptive and can identify anomalous shapes of $\boldsymbol{L}(\theta_{RS})$ for the pixels where the variance in $[\theta_{RS}]$ v/s $[-\Delta\theta_{RS}/\Delta t]$ may be high. For this study, we divide the dynamic range of the observed θ_{RS} into four quantiles (P=$\{p_i\}$, i=1 to n, n=4), and the mean and variance of $[-\Delta\theta_{RS}/\Delta t]$ for each quantile is calculated. Pixels with less than 100 drydown samples or with any θ_{RS} partition with less than 20 samples are not used for the analysis to ensure enough data points for a reliable statistical analysis.

A two tailed Welch's t- test (Welch, 1947) is used to compare the mean values of $[-\Delta\theta_{RS}/\Delta t]$ for the subsequent partitions (p_i v/s p_{i-1}, i=2 to 4) with the null hypothesis of equal mean at a significance level of 0.05. Welch's t- test is used in this analysis for its suitability in conditions where the assumptions of normality and homogeneity of sample variance cannot be applied (Mellinger, 2016; Rasch et al., 2009; YUEN, 1974). The t-statistics for the test is defined as follows:

$$t = \left(\frac{\overline{\mu}_{p_i} - \overline{\mu}_{p_{i-1}}}{\sqrt{\frac{{\sigma_{p_i}}^2}{n_{p_i}} + \frac{{\sigma_{p_{i-1}}}^2}{n_{p_{i-1}}}}} \right) \tag{1}$$

where n_{p_i}, $\bar{\mu}_{p_i}$ and σ_{p_i} are the number of available data points, mean and standard deviation of the $[-\Delta\theta_{RS}/\Delta t]$ for partition p_i, where i=2 to 4.

From Eq. (1) we observe that the canonical shape, S, of the loss function $\boldsymbol{L(\theta_{RS})}$ is dependent on the mean and variance of $[-\Delta\theta_{RS}/\Delta t]$ within each partition. Hence, S can be written as, S=$f(\mu_P, \sigma_P)$, where P is the superset of all θ_{RS} partitions. For n =4, S can take any of 27 possible shapes, and is denoted with a unique ternary combination of C, F and R (**Figure** 1) in the order of decreasing θ_{RS}. A ternary notation S= (FCF), for example, represents a F-rate of moisture loss in initial phase of soil drydown, followed by C- and F-rate of loss with further drying of soil. For brevity, any repeated/continued drydown processes of similar phase is abbreviated only once (e.g., CCF is denoted as CF).

The entire sample space of $[-\Delta\theta_{RS}\Delta t]$ for a pixel is an ensemble of samples from tens of drydown events (each ranging from a few to multiple days) distributed within different quantiles of θ_{RS} (**Figure** 1). Hence, the sample points within each θ_{RS} quantile may be assumed to be independent. The estimates of $[-\Delta\theta_{RS}\Delta t]$ are prone to sampling error due to the retrieval conditions, flagging and accuracy, which can influence the shape of $\boldsymbol{L}(\theta_{RS})$. A resampling approach is used to estimate the mean and variance of $[-\Delta\theta_{RS}\Delta t]$ from each θ_{RS} partition. The shape of drydown for individual footprint is estimated as

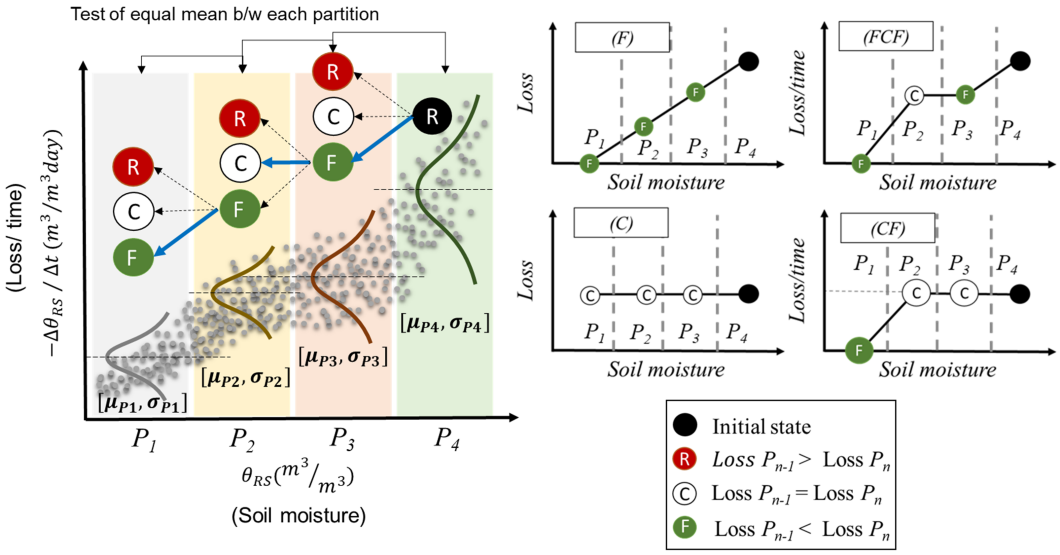

Figure 1. A conceptual representation of the non-parametric method for estimation of a-priori shapes of the soil moisture loss function, $\boldsymbol{L}(\theta_{RS})$. The mean rate of loss for each partition of soil moisture range is compared using Welch's t-test for subsequent partitions. A few sample shapes of $\boldsymbol{L}(\theta_{RS})$ is shown in the figure (right panels).

$s_r = f\left(\mu_{(P,r)}, \sigma_{(P,r)}\right)$, where $\mu_{(P,r)}$ and $\sigma_{(P,r)}$ are the realizations of the mean and variance of the r^{th} resample (with replacement) of $[-\Delta\theta_{RS}/\Delta t]$ from each θ_{RS} partition. A total of 1000 resamples are used for estimating s_r, providing estimates of canonical shapes of $\boldsymbol{L}(\theta_{RS})$ as $S_R = s_1, s_2, s_3, \ldots., s_{1000}$. S_R is a vector containing the estimated canonical shapes of $\boldsymbol{L}(\theta_{RS})$ for each set of resampled observations. For each pixel, the mode of S_R and its corresponding probability mass function is obtained. These two terms provide the Most Probable Shape (MPS) and Probability of Realization (PR), representing most likely shape of drydown curve with the relative confidence for the pixel, respectively. Globally significant MPS (each covering >1% of evaluated pixels) are selected as a-priori shapes which are parameterized using a least-squares, piecewise curve fit on $[-\Delta\theta_{RS}\Delta t]$ v/s $[\theta_{RS}]$ observations.

3.2 Step 2: Seasonal fitting of piecewise parametric models for $\boldsymbol{L(\theta_{RS})}$

All selected a-priori shapes obtained in Step 1 are fitted on the samples of $[-\Delta\theta_{RS}\Delta t]$ vs $[\theta_{RS}]$ using a pixel-wise least-squares approach previously used in some recent studies (Akbar et al., 2018; Schwingshackl et al., 2017). The parameters for the shapes are optimized in R using a non-linear least-squares (NLS, Pollard and Radchenko (2006)) method with parameter bounds based on Levenberg-Marquardt (Moré, 1978) algorithm. The parameter bounds are used to avoid unrealistically large or small value of the fitting parameters. The curve-fitting follows a (n*k) resampling and cross-validation approach, where n is the number of resamples (with replacement) from the observations used for model development, followed by a k-fold validation (Arlot & Celisse, 2010; Kohavi et al., 1995). For fitting the canonical shapes, the study uses n=25 and k=10, providing 250 estimates of the model parameters for each canonical shape for every pixel. To capture the seasonal influence on the SM dynamics at the RS footprint scale, the seasonal values of $[-\Delta\theta_{RS}/\Delta t]$ vs $[\theta_{RS}]$ data are used to fit the canonical shapes. Seasons are defined in monthly triplets as December-February (DJF); March-May (MAM); June-August (JJA); and, September-November (SON). Three performance indices are used to evaluate the model fit, namely, Willmott's index of agree-

ment (d) (Willmott et al., 2011), Coefficient of correlation (CC) and Mean squared error (MSE, in m^6/m^6/day.). Willmott's index (d) provides better sensitivity to the additive and proportional differences in the observed and estimated means and variances compared to CC. Values of d and CC close to 1 indicate a perfect fit while perfect score for MSE is 0.

Initially, the canonical form with the least mean MSE (for 250 model fits) is selected as the best fitting (representative) pathway of the SM drydown for the pixel. In a case where the mean MSE of a simpler (with lesser parameters) canonical form falls within the 95% confidence interval of the mean MSE of the best-fitting shape, then the new canonical form replaces the complex shape as the representative drydown pathway for the pixel. This way, preference is given to simpler canonical shapes with reasonable performance to minimize the risk of over parameterization.

3.3 Variability index for the mean inter-seasonal deviation in drydown parameters

The inter-seasonal variability in the soil drydown parameters is captured using a Variability Index (VI) as follows:

$$VI(\%) = \frac{100}{N} \sum_{i=1}^{N} \frac{|(P_i - \bar{P})|}{\bar{P}} \tag{2}$$

where N= number of seasons i.e. 4, $\bar{P}$ is the seasonal average value of the drydown parameters, P_i is the value of the parameter for season i where i=1 to 4. Higher values of VI (expressed in percentage) indicate stronger inter-seasonal variability in the estimated values of the parameter compared to the mean value for the four seasons. The index is similar in formulation to the seasonality index used by (Walsh & Lawler, 1981; Troch et al., 2013) to evaluate the seasonal variability in the precipitation at a monthly time-step.

4 Results and discussion

4.1 Non-parametric shapes of global θ_{RS} drydown

The non-parametric approach (described in Section 3.1) is used to obtain the MPS and PR for each pixel. Dominant global shapes are obtained based on a frequency analysis for MPSs for all pixels. We observe that six canonical shapes represent θ_{RS} drydowns for 99.14% of the evaluated pixels across the globe. These shapes are F (／), FC (／), FCF (⌒) and CF (⌒) which cover 40.12%, 15.58%, 16.48% and 20.45% of the global pixels respectively (**Table** 1).

Shapes C (−) and CFC (⌒) are found to be dominant in 2.28% and 4.23% pixels. Four case studies: North America, India, Africa and Australia (**Figure** 2) show that the dominant land use and aridity patterns are reflected broadly by the spatial variability in the shapes of $\boldsymbol{L(\theta_{RS})}$. A clear ecosystem/climate-based divide is evident in the case of North America (**Figure** 2a), where predominantly arid and semi-arid regions of the U.S. Southwest and Mexico show a linearly decreasing, F-shaped (／) $\boldsymbol{L(\theta_{RS})}$. The croplands in the U.S. mid-west display a wider range of dominant hydrological processes due to excessive irrigation and/or precipitation, leading to moisture rich conditions. Hence, FCF (⌒) shape is observed predominantly for the croplands in US mid-west. India can be regionalized in three distinct groups (**Figure** 2b)- i) warm and humid east (with CF-shaped (⌒) drydown), ii) dry west and central India (FC-shaped (／) drydown), and iii) Northern plains and parts of southern India with moderate rainfall (with F-shaped (／) drydown). In Africa, the transition from rainforests to savanna and grasslands is evident as the shape of $\boldsymbol{L(\theta_{RS})}$

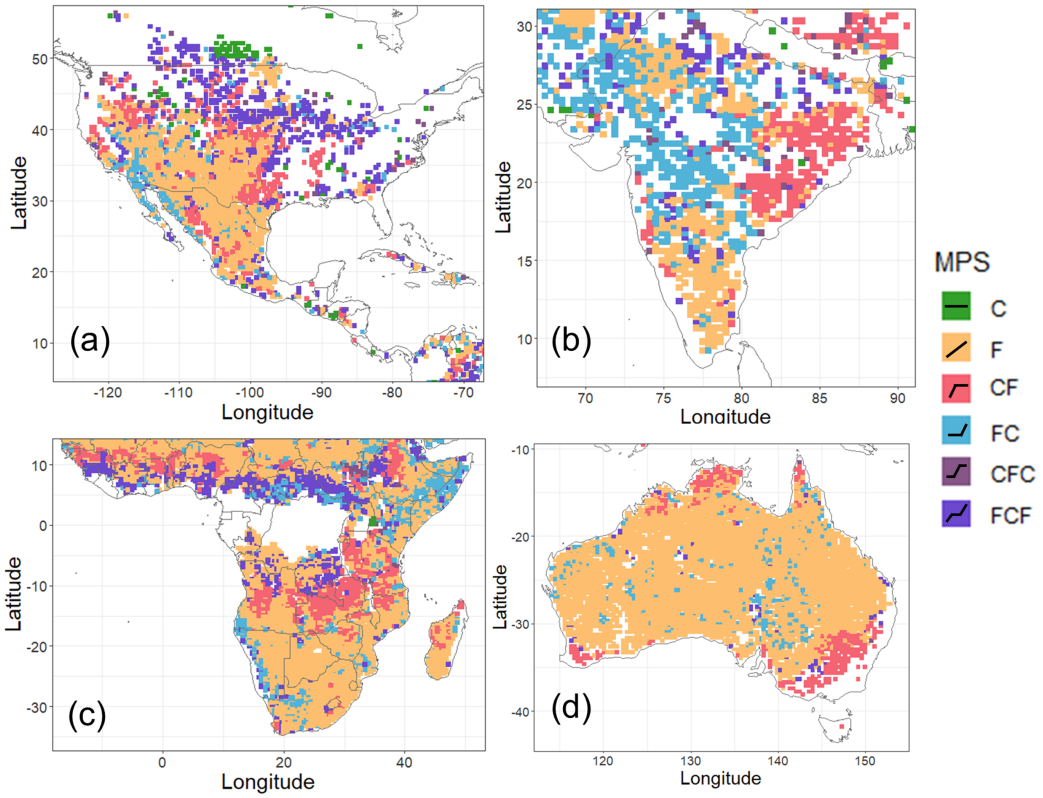

Figure 2. Distribution of the Most Probable Shapes (MPS) of the surface soil moisture loss function $\boldsymbol{L}(\theta_{RS})$ for (a) North-America, (b) India (c) Africa and (d) Australia.

changes from predominantly FCF (⌐) to CF (⌐) and F (/) with the decrease in the overall moisture availability (**Figure** 2c). Similarly, the temperate and humid regions (shape CF i.e. ⌐) in Australia can be distinguished from the arid interiors (F and FC) (**Figure** 2d). The shape FC (/) is observed only in the arid parts of Africa (Ethiopia, Somalia and Namibia), regions adjoining the Gulf of California (Baja California Peninsula), western and central India, and some parts of central Australia. The spatial distribution of the shapes of SM drydown for the Contiguous U.S. obtained by the non-parametric approach (**Figure** 2a) resemble the SM drydown shapes evaluated by (Akbar et al., 2018). However, a global analysis using the non-parametric approach reveals one more shape, CFC (⌐), as one of the dominant shapes of SM drydown compared to the six shapes proposed by Akbar et al. (2018). Moreover, seasonal fitting of the drydown pathways reveal spatially variability in the drydown pathways (and respective parameters) as explained in the later sections.

4.2 Parametric fitting of seasonal drydown pathways

The proposed a-priori canonical shapes of $\boldsymbol{L}(\theta_{RS})$ by the non-parametric approach conform to the functional from of SM drydown previously proposed based on fine-scale studies (Guswa et al., 2002; Laio et al., 2001; Rodriguez-Iturbe, 2000) as shown in (**Figure** 3). SM drydown can be assumed to be a four-phase/regime process consisting of gravity drainage (G), energy-limited ET-driven drydown (W), water-limited ET-driven drydown (T), and soil evaporative drydown (D) phase/regime (**Figure** 3a). The intersection points between two consecutive drydown regimes (θ^{GW}, θ^{WT} and θ^{TD}) represent the SWRP_{eff} (field capacity, critical point and wilting point respectively) for the RS footprint. If $\theta_{RS} > \theta^{GW}$,

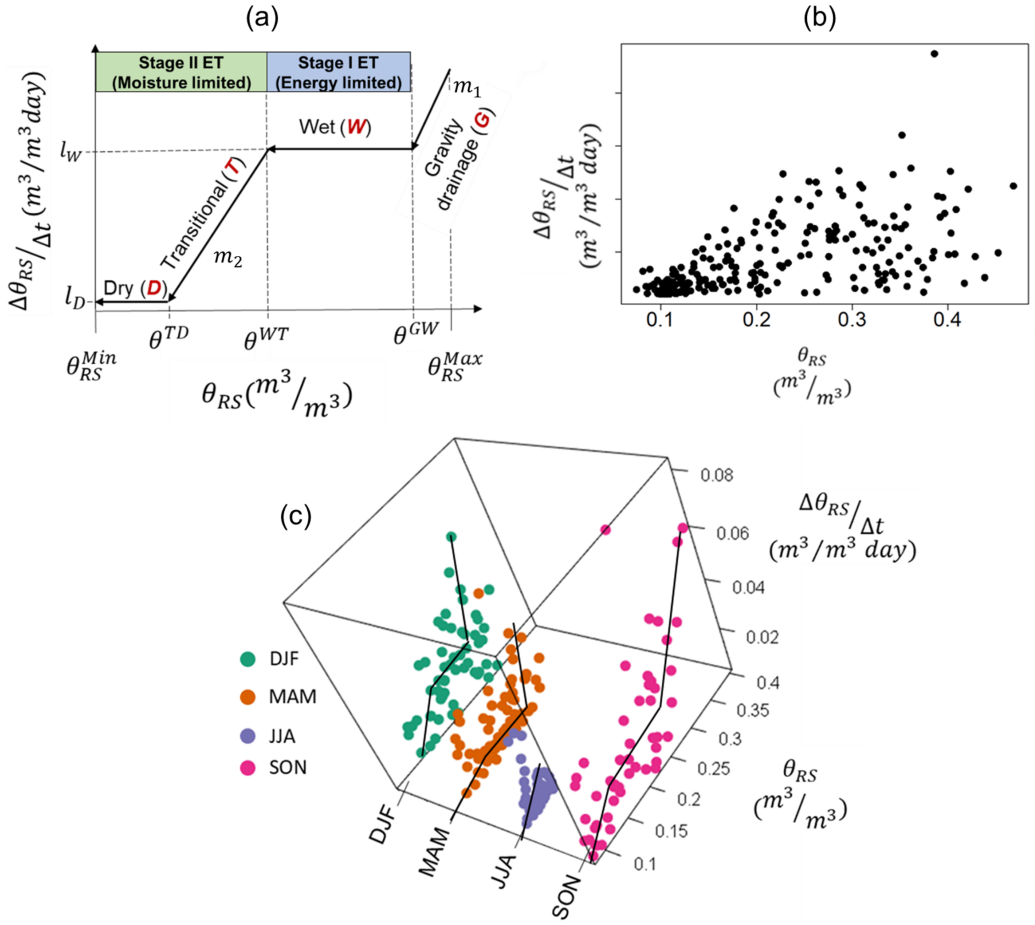

Figure 3. ***a)*** A typical soil moisture loss function, $\boldsymbol{L(\theta_{RS})}$ at the remote sensing scale. The dry, wet, transitional and gravity drainage phase in $\boldsymbol{L(\theta_{RS})}$ are identified as *D, W, T* and *G* respectively. θ^{GW}, θ^{WT} and θ^{TD} represent the intersection between the gravity drainage and wet phase, wet and transitional phase, and transitional to dry phase respectively and are called the effective SWPs for the respective pixel. m_1 and m_2 are the slope of $\boldsymbol{L(\theta_{RS})}$ during gravity drainage and transitional phase respectively. If $\theta_{RS} > \theta^{GW}$, SM loss is dominated by gravity drainage. Between θ^{GW} and θ^{WT}, the soil reaches an energy deficient stage and the rate of loss is referred to as l_W. The stage between θ^{TD} and θ^{WT} is referred to as the transitional phase where soil reaches moisture deficit conditions. The last limb of $\boldsymbol{L(\theta_{RS})}$ is the stage of near-zero values of $\boldsymbol{L(\theta_{RS})}$ indicating dry soil conditions with low, but near-consistent loss of soil moisture in the pixel (l_d). ***b)*** Observed soil moisture drydown i.e. [θ_{RS}] v/s [$-\Delta\theta_{RS}/\Delta$t] for a SMAP pixel ***c)*** Representation of the seasonal soil moisture drydown for a pixel. Seasonal dimension in the analysis help reduce scatter and provides discernable patterns in the [θ_{RS}] v/s [$-\Delta\theta_{RS}\Delta$t].

then SM loss is dominated by gravity drainage. Between θ^{GW} and θ^{WT}, the soil reaches an energy-limited (Stage I evapotranspiration) regime with a near-constant rate of loss, l_w. The phase between θ^{WT} and θ^{TD} is referred to as the transitional phase where the pixel reaches moisture deficit regime (Stage II evapotranspiration). The last limb of $\boldsymbol{L(\theta_{RS})}$ is the stage of near-zero values of $\boldsymbol{L(\theta_{RS})}$ indicating dry conditions with low, but near-constant loss of θ_{RS} by soil evaporation (with no plant available water). The slope of the gravity drainage and the transitional limbs of $\boldsymbol{L(\theta_{RS})}$ are indicated by m_1 and m_2 respectively. (**Figure** 3b) provide an example of $[\theta_{RS}]$ v/s $[-\Delta\theta_{RS}/\Delta t]$ observations from a sample SMAP pixel. At RS-footprint scale, temporal variability in the land-surface heterogeneity, and atmospheric and hydrologic drivers of θ_{RS} may be significant. Hence, expanding the $[\theta_{RS}]$ v/s $[-\Delta\theta_{RS}/\Delta t]$ relationship in a seasonal dimension helps capture the seasonally dominant processes/regimes in the pixel (**Figure** 3c).

4.2.1 Identification of physical processes

The mathematical formulation of the six selected canonical shapes for season-wise fitting of $\boldsymbol{L(\theta_{RS})}$ is provided in **Table** 1. As the non-parametric approach does not distinguish between pathways *i*) wet {W} and dry {D}, *ii*) gravity drainage {G} and transient {T}, and *iii*) transient to dry {TD} and gravity drainage to wet {GW}, certain threshold values of θ_{RS} or drydown parameters are determined to distinguish drydown pathways with the same shape. Pathway {C} is classified as {D} if constant-rate loss is less than 0.008 m^3/m^3/day, otherwise the pathway is identified as {W}. The threshold (0.008 m^3/m^3/day) is selected based on the trough of the bimodal distribution of the global constant-rate losses prior to process identification. Falling-rate process is classified as G if $\theta^{GW} \geq 0.15\text{m}^3/m^3$. The threshold of θ_{RS}=0.15 m^3/m^3 is suggested by some other studies to demarcate the energy-limited regime (Akbar et al., 2018; Schwingshackl et al., 2017; Shellito et al., 2018). If transition from falling-rate to constant-rate occurs at $\theta_{RS} \geq 0.15\text{m}^3/m^3$, shape {FC} is classified as pathway {GW}.

4.2.2 Spatial distribution of the seasonal drydown pathways

Seasonal availability of moisture and energy dictates the soil hydrologic regimes and pathways of θ_{RS} drydown for each season as shown in **Figure** 4. For example, due to moisture-rich conditions and low temperatures during DJF, θ_{RS} drydown in the eastern U.S. is dominated by pathway {W}. However, multiple regimes like {WT} and {WTD} are observed with the reduction of mean SM (and increase in temperatures) during the summer season (JJA). For the Southeastern Asian regions receiving monsoonal precipitation in JJA, the drydown pathways are predominantly {W}. However, other regimes are observed as the soil loses moisture after the end of the precipitation season. Depending on the climatology, similar observations can be made for several other regions like western Australia ({TD} in SON v/s {WTD} and {WT} in JJA), North-eastern Brazil ({TD} and {D} in JJA- SON v/s {WT} and {WTD} in DJF- MAM), Savannah grasslands of Central Africa and most parts of Western Europe ({W} in DJF v/s {WTD}, {TD} and {D} in JJA).

Pathway {TD} is observed primarily in the arid and some parts of semi-arid climate due to high temperatures and general scarcity of moisture. Similarly, {T} is found to be in dominant in 3.7-4.4 % (depending on the season) of the pixels, predominantly in arid climate. Pathway {W} is observed in greater proportion in humid and dry-sub-humid climates due to presence of moisture-rich conditions. Gravity-drainage pathway {G} is rarely observed and hence is not observable in **Figure** 4. The biggest percentage of global SM drydown can be attributed to shape {GWT} and WT which contribute to more than half of the observed global SM drydowns (24.4-26.2% and 25.1-29.9% respectively, depending on the season). Shapes {CF}, {CFC} and {C} contribute to 18-19.5%, 11.3-13.6% and 8.3-12.4% respectively. Pathway {WTD} is observed in larger fraction for the regions at the intersection between arid and humid ecosystems. More complex shapes are replaced with

Table 1. Mathematical representation of the globally dominant pathways of SM drydown.

Shape	Pathway	Parameters	Equation	Form
{C}	Wet (**W**) Dry (**D**)	1	$-\Delta\theta_{RS}/\Delta\mathrm{t} = l_w$, for all θ_{RS} $-\Delta\theta_{RS}/\Delta\mathrm{t} = l_d$, when $-\Delta\theta_{RS}/\Delta\mathrm{t} < 0.008 m^3/m^3/day$	
{F}	Transitional (**T**) Gravity drainage(**G**)	2	$-\Delta\theta_{RS}/\Delta\mathrm{t} = m_2\left(\theta_{RS} - \theta^{TD}\right)$, for all θ_{RS} $-\Delta\theta_{RS}/\Delta\mathrm{t} = m_1\left(\theta_{RS} - \theta^{GW}\right)$, when $\theta^{GW} \geq 0.15\ m^3/m^3$	
{CF}	Wet & transitional (**WT**)	3	$-\Delta\theta_{RS}/\Delta\mathrm{t} = m_2\left(\theta_{RS} - \theta^{TD}\right)$, for $\theta_{RS} < \theta^{TD}$ $-\Delta\theta_{RS}/\Delta\mathrm{t} = m_2\left(\theta^{WT} - \theta^{TD}\right)$, for $\theta_{RS} \geq \theta^{WT}$	
{FC}	Transitional & dry (**TD**) Gravity drainage & wet (**GW**)	2	$-\Delta\theta_{RS}/\Delta\mathrm{t} = l_d$, for $\theta_{RS} \leq \theta^{TD}$ $-\Delta\theta_{RS}/\Delta\mathrm{t} = l_d + m_2\left(\theta_{RS} - \theta^{TD}\right)$, for $\theta_{RS} \geq \theta^{TD}$ $-\Delta\theta_{RS}/\Delta\mathrm{t} = l_w$, for $\theta_{RS} \leq \theta^{GW}$ $-\Delta\theta_{RS}/\Delta\mathrm{t} = l_w + m_1\left(\theta_{RS} - \theta^{GW}\right)$, for $\theta_{RS} \geq \theta^{GW}, \theta^{GW} \geq 0.15 m^3/m^3$	
{CFC}	Wet, transitional & dry (**WTD**)	4	$-\Delta\theta_{RS}/\Delta\mathrm{t} = l_d$, for $\theta_{RS} \leq \theta^{TD}$ $-\Delta\theta_{RS}/\Delta\mathrm{t} = l_d + m_2\left(\theta_{RS} - \theta^{TD}\right)$, for $\theta^{TD} \leq \theta_{RS} \leq \theta^{WT}$ $-\Delta\theta_{RS}/\Delta\mathrm{t} = l_d + m_2\left(\theta^{WT} - \theta^{TD}\right)$, for $\theta_{RS} > \theta^{WT}$	
{FCF}	Gravity drainage, wet & transitional (**GWT**)	5	$-\Delta\theta_{RS}/\Delta\mathrm{t} = m_2\left(\theta_{RS} - \theta^{TD}\right)$, for $\theta_{RS} \leq \theta^{WT}$ $-\Delta\theta_{RS}/\Delta\mathrm{t} = m_2\left(\theta^{WT} - \theta^{TD}\right)$, for $\theta^{WT} \leq \theta_{RS} \leq \theta^{GW}$ $-\Delta\theta_{RS}/\Delta\mathrm{t} = m_1\left(\theta_{RS} - \theta^{GW}\right)$, for $\theta_{RS} > \theta^{GW}$	

m_1 = slope of gravity drainage phase; m_2 = slope of transitional phase; l_w= drydown rate at potential evapotranspiration; l_d= $-\Delta\theta_{RS}/\Delta\mathrm{t}$,when $\theta_{RS} \leq \theta^{TD}$; F=falling-rate loss, C=constant-rate loss

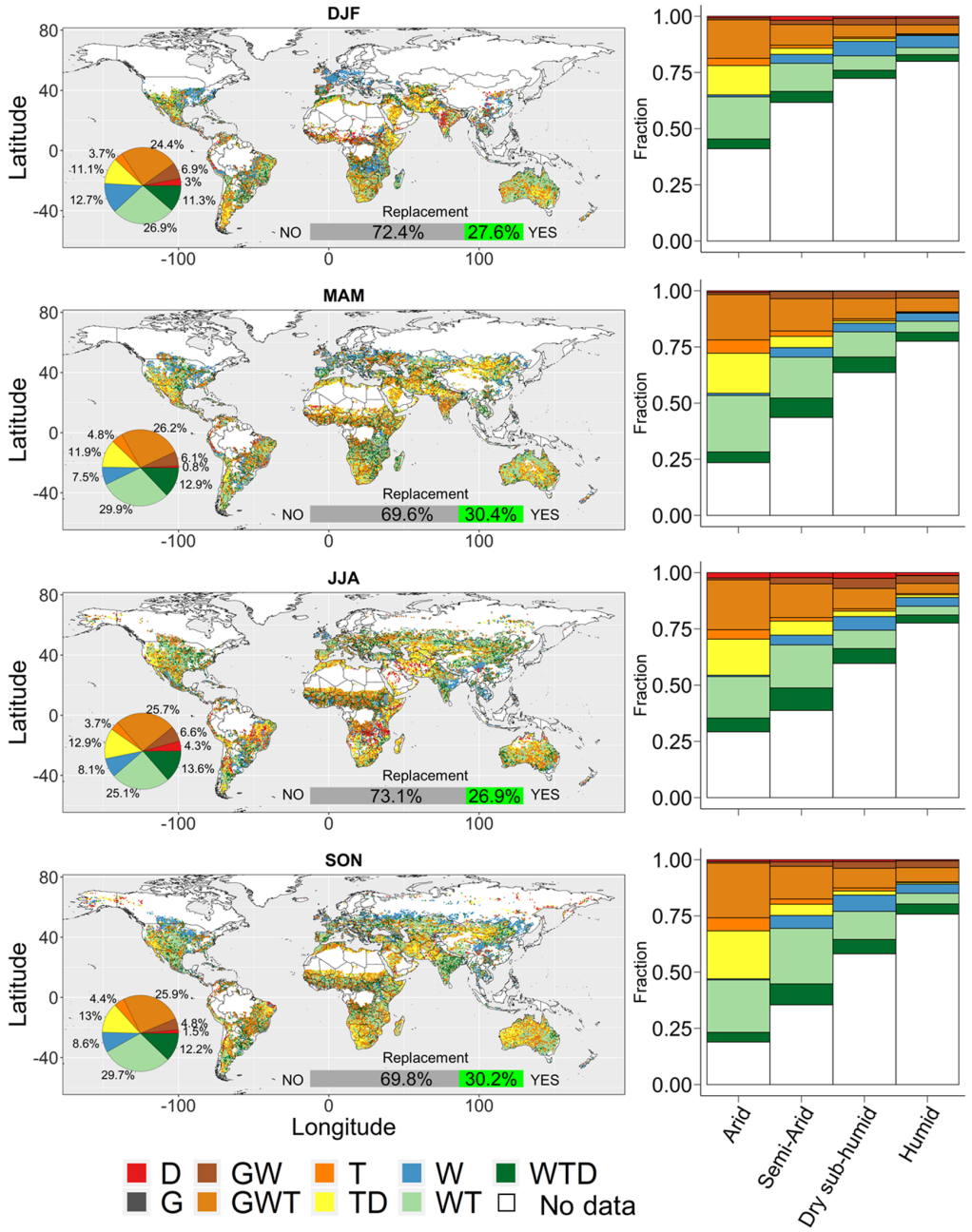

Figure 4. (*Left panel*) Selected shapes of the seasonal surface soil moisture loss function $\boldsymbol{L}(\theta_{RS})$. The inset pie chart shows the percentage spatial distribution of the canonical forms of $\boldsymbol{L}(\theta_{RS})$. The horizontal bar at the bottom of the figure shows the percentage of pixels where the canonical form of $\boldsymbol{L}(\theta_{RS})$ was replaced by a simpler canonical form with lesser parameters. Fraction of green color represents the global percentage of pixels where replacement was carried out. (*Right panel*) Fractional coverage of each drydown pathway for different climate types. White color shows pixels not used in the analysis.

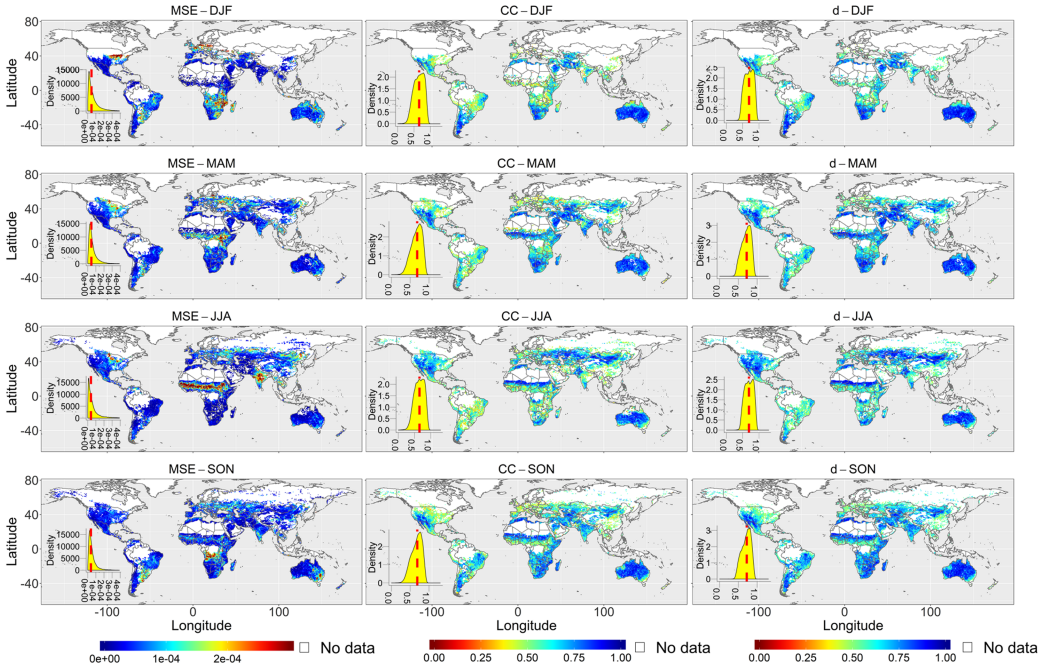

Figure 5. Performance evaluation of the seasonally fitted canonical forms of $\boldsymbol{L(\theta_{RS})}$ using three indices namely Mean Squared Error (MSE, in $m^6/m^6/day^2$), Coefficient of correlation (CC, dimensionless) and Willmott's index of agreement (d, dimensionless). The inset shows the probability density function of each performance indicator, with the dotted red line indicating the median value of the distribution. Due to constant value of fitted $[-\Delta\theta_{RS}/\Delta t]$, CC and d statistics for the pathway {W} and {D} cannot be calculated and only MSE for such pixels is reported. White color represents pixels not used in the analysis.

simpler shapes (with lesser parameters) at about 27.6, 30.4, 26.9 and 30.2% of the evaluated global pixels for DJF, MAM, JJA and SON months, respectively.

4.2.3 Performance assessment of parametric model fit

Figure 5 shows the global spatial distribution of the performance indices of the model fit for $\boldsymbol{L(\theta_{RS})}$. The overall performance of the model fits is found to be satisfactory with the overall mean global value of d, CC and MSE to be approximately 0.7, 0.65 and 0.00006 $m^6/m^6/day^2$, respectively. A strong seasonal variability is observed in the spatial distribution of the mean MSE across the globe, especially for croplands, grasslands, and savannas (CGS). Overall, sparsely vegetated regions and shrublands show lower mean MSE in the model fit compared to CGS owning to a smaller range of $[-\Delta\theta_{RS}/\Delta t]$. Standard deviation of the estimated parameters is provided in **Figure S1-3** of the Supplementary material.

Certain global hotspots of relatively low fitting performance of $L(\theta_{RS})$ can be observed (**Figure** 5) in Sahel region (Africa), U.S. Mid-West, Central India and Northern Europe all predominantly CGS ecosystems. Patchy vegetation (Moustakas et al., 2009) and/or variable precipitation/irrigation patterns within the RS-footprint in CGS ecosystems lead to high subgrid heterogeneity within the RS-footprint, causing several simultaneous and independent subgrid-scale drydown (or possibly wetting, in some instances) processes. Hence, a non-unique relationship between the mean θ_{RS} and the effective values of $[-\Delta\theta_{RS}/\Delta t]$ for

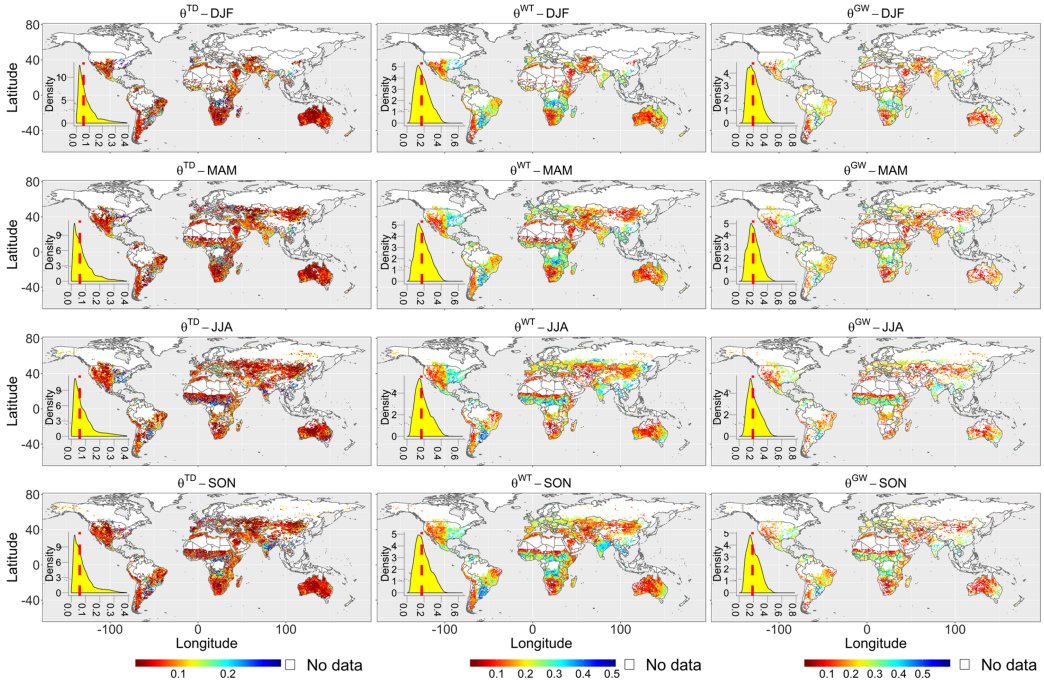

Figure 6. Spatial distribution of θ^{TD}, θ^{WT} and θ^{GW} (in m^3/m^3). The inset shows the probability distribution function (PDF) of the seasonal estimates of the respective parameter. Red line in the PDF indicate the median value. White color represents pixels not used in the analysis.

the RS-footprint may be observed increasing the likelihood of misidentification of the shape of $\boldsymbol{L(\theta_{RS})}$ in CGS ecosystems. A decrease in the retrieval accuracy of SMAP with the increased VWC and reduction in the surface temperature due to vegetation induced evapotranspiration and shade especially in the growing season, further impacts the effective θ_{RS} drydown observed at the RS-footprint scale. However, a detailed analysis of the impact of vegetation growth on the SM drydowns at large spatial scales in CGS landscapes is beyond the scope of the current study.

4.3 Global parameters and controls of seasonal $\boldsymbol{L(\theta_{RS})}$

4.3.1 Soil water retention parameters

The three SWRP$_{eff}$ (θ^{TD}, θ^{WT} and θ^{GW}) indicate the transition points between the dominant hydrologic regimes of the SM drydown process. The spatial distribution of the seasonal SWRP$_{eff}$ is shown in **Figure** 6. The distribution of θ^{TD} is observed to be right skewed with high values (>0.2 m^3/m^3) for regions like Central India, parts of south Brazil and adjoining regions, Central Africa and parts of Southeastern US all regions with high percentage (>40%) of clay content in the soil. A clear climate-based divide is observed in the values of θ^{WT} and θ^{GW}. The mid-latitude regions in South America and Africa, Eastern U.S. and Eastern Asia can be distinguished for high value of θ^{WT} and θ^{GW} compared to the adjoining regions with semi-arid and arid climates.

In general, θ^{TD} show a higher inter-seasonal variability compared to θ^{WT} and θ^{GW}. The seasonal variability in the SWRP$_{eff}$ is observable with higher clay fraction as some clayey soils are prone to shrinking and swelling, which adversely affects the water retention due to preferential flow through cracks as seen in several field-scale studies (Boivin, 2011;

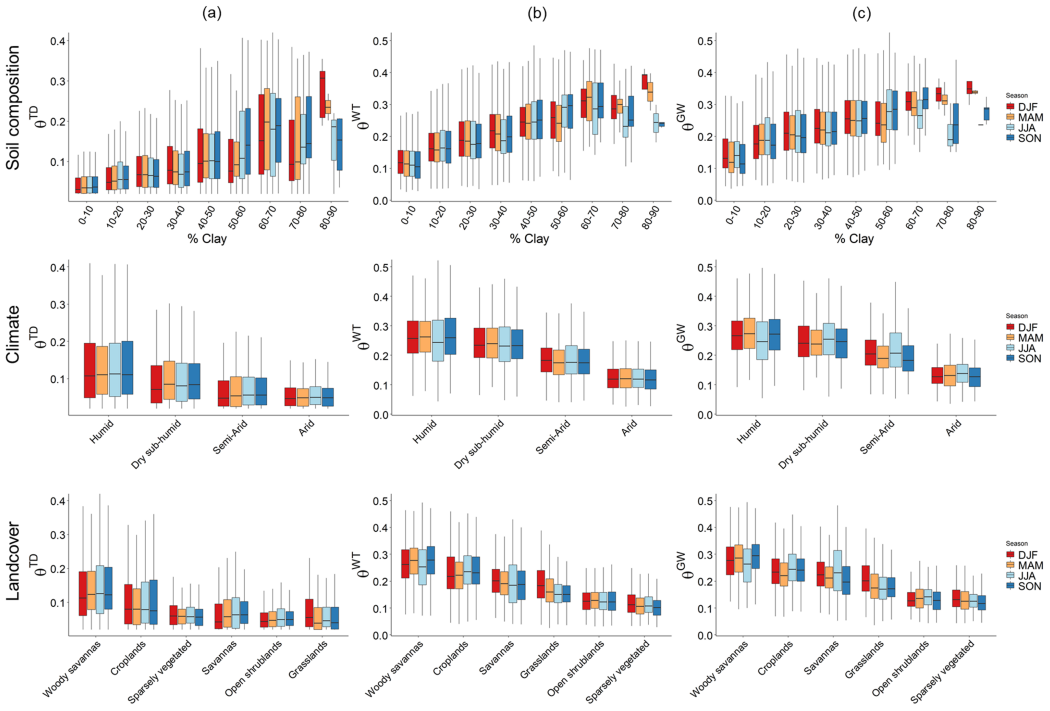

Figure 7. Boxplots summarizing the seasonal values of the SWRP_{eff} i.e. ***a***) θ^{TD},***b***) θ^{WT} and ***c***) θ^{GW} for soil composition (%clay), climate and landcover classes.

Boivin et al., 2004; Warkentin, 1962). Such observation can be made for Texas, U.S., Central India, and Pampas of South America where a high seasonal variability in the values of θ^{TD} is observed over the seasons. Fine-scale studies report an increase in the plant available water content of the soil with increase in clay and loam fraction (Kirkham, 2005). Due to finer particle size of clayey soils, water is held more strongly due to the adhesive (water and soil particles) and cohesive (water-to-water) forces in the soil matrix compared to sandy soils (Hillel, 2012). Similar observations can be made in **Figure** 7 where an increasing percentage of clay in the soil leads to increase in θ^{TD}, θ^{WT} and θ^{GW} for all seasons. However, as the moisture content of the pixel increases, the effective θ_{RS} dynamics become increasingly dependent on the subgrid-scale variability in the SM due to land-surface heterogeneity (vegetation, topography and precipitation patterns etc.), rather than the soil composition. This effect is more pronounced for humid, and dry sub-humid climates with croplands, savannah and grasslands landcovers with high clay content (>40%) leading to high variance in the observed patterns of SWRP_{eff} for the respective clay content, landcover and climate classification as shown in **Figure** 7.

However, a partial cause of the high variability in the SWRP_{eff} v/s clay fraction relationship in **Figure** 7 can be the uncertainties in the soil textural class estimates, and upscaling of this information from finer scale to RS-footprint scale. The estimates of soil texture depend on the availability and uncertainty in the soil-geographical data and environmental covariates, which may be high and can significantly impact the analysis (Batjes, 2016; Folberth et al., 2016; Small et al., 2014), more so, at a global scale. Subpixel-scale variability in the soil properties may impact the effective manifestation of the pixel-scale SWRP_{eff} due to the non-linear control of the soil properties on the soil water retention (Mohanty & Skaggs, 2001). The influence of various non-linear upscaling schemes (Mohanty

& Zhu, 2007) of soil textural properties in capturing the $SWRP_{eff}$ at RS-footprint scale is not explicitly explored and is beyond the scope of the current analysis.

4.3.2 Falling-rate losses (m_1 and m_2)

The rate of loss of SM during the gravity drainage phase is indicated by m_1. High m_1 is observed in *i*) southern Africa, parts of Australia and southern parts of South America during DJF, *ii*) parts of Central Asia and southern Africa during MAM, *iii*) Sahel and U.S. Southwest during JJA, and *iv*) most parts of Australia and southern Africa in SON. High values of m_1 in different ecosystems may be the result of very different processes. For African Savannah, m_1 is found to be high during the beginning of the wet season due to increase in unsaturated hydraulic conductivity after the precipitation season (May-December) with an increased availability of moisture. However, low organic matter and high sand content in pixels in the arid climate may lead to poor moisture retention in soils and hence, rapid drainage as found in several studies (Ankenbauer & Loheide, 2016; Saxton & Rawls, 2006). Also, subpixel-scale variability in the precipitation, surface runoff and landscape characteristics within the large scale of evaluation (36 km) may lead to differential rate of drainage across the pixel leading to underestimation of the effective drainage losses for the pixel (Akbar et al., 2018)).

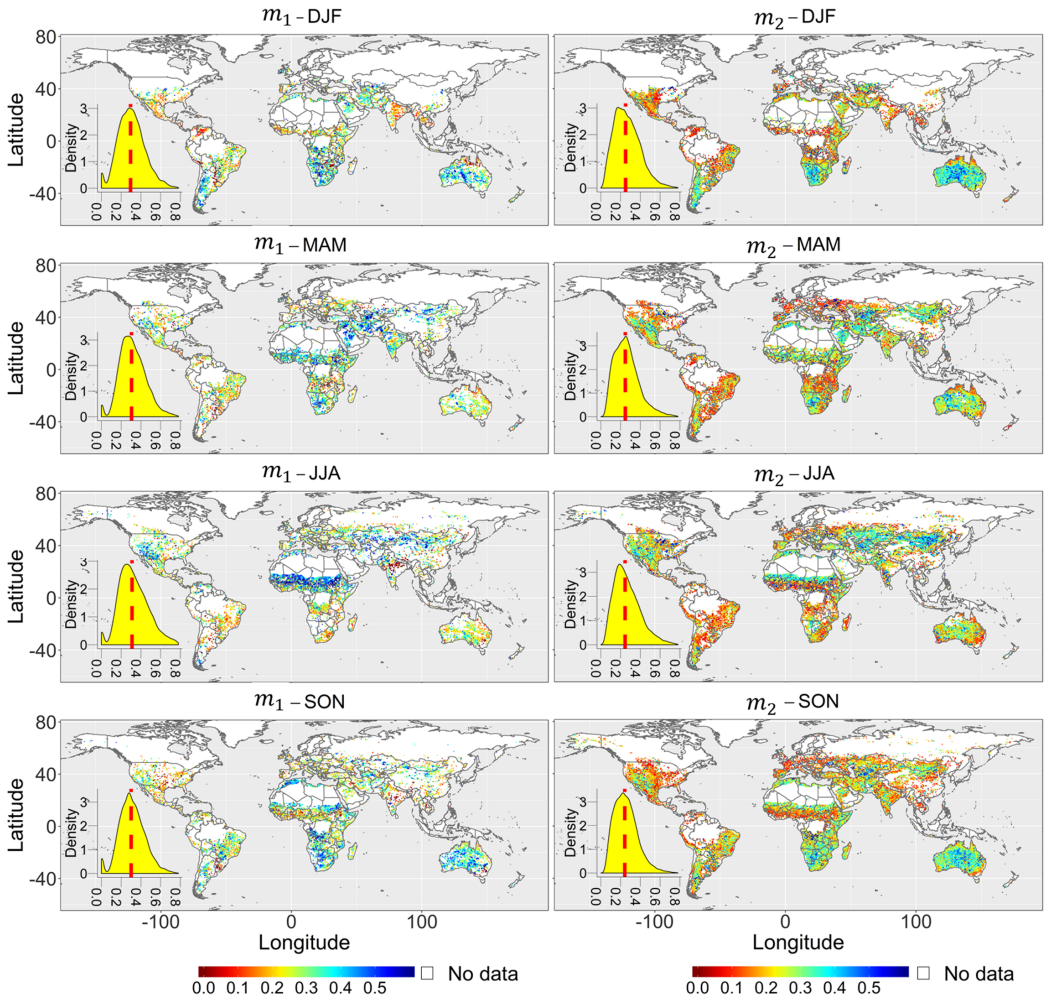

Figure 8. Same as Figure 6, for m_1 and m_2 (day^{-1}).

In the transitional phase (moisture limited condition) SM exerts the limiting control over latent heat flux and is the primary factor controlling evapotranspiration instead of the net radiation (Dirmeyer, 2011; Santanello et al., 2018). The slope of the transitional phase of $\boldsymbol{L(\theta_{RS})}$ i.e. m_2, represents the strength of the terrestrial component of the land-atmospheric coupling, with high m_2 value representing higher SM-driven variance in evapotranspiration in response to the atmospheric moisture demand. Seasonal variability in the Potential Evapotranspiration (PET, **Figure S4** of the Supplementary material) is observed to be the key driver of the seasonal spatial patters of m_2, especially for the arid and semi-arid climates. High PET values in most parts of Australia, southern Africa and Patagonia region of South America (**Figure S4**) show high values of m_2 in austral spring and summer (SON and DJF respectively) as shown in **Figure** 8. However, with the progression of late spring and summer in the northern hemisphere (MAM and JJA), U.S. Southwest and large parts of Mexico, Indus valley, Guinea coast and Horn of Africa, and Central Asia show an increase in m_2. Compared to arid/semi-arid climates, humid and sub-humid ecosystems operate at a larger dynamic range of SM. Strong connectivity of surface and root zone profile in humid and sub-humid ecosystems facilitates upward movement of moisture due to increased matric suction with loss of θ_{RS}, thus dampening the rate of drydown (smaller m_2). Hence, if the atmospheric moisture demand isn't sufficiently high (as in the case of eastern U.S. and western Europe in SON, Southern Brazil and parts of Argentina in MAM- JJA, Southern U.S. and Mexico in DJF), SM is retained for a longer period within the pixel leading to a smaller value of m_2 i.e. greater memory of SM (Koster & Suarez, 2001) as shown in **Figure** 8. In some regions like Eastern India (post monsoonal vegetation growth in SON) and savannah/ grasslands of Sahel region (in SON), vegetation has a strong influence on the values of m_2. High transpiration from plants due to access to deeper profile SM may contribute to development of a strong vegetation-atmosphere coupling (Zscheischler et al., 2015) which reduces the limiting control of surface SM on evapotranspiration, leading to lower m_2 values.

Spatial and temporal variability in m_2, as shown in **Figure** 8, is similar to the results obtained by (Dirmeyer, 2011) who used simulated SM simulations for the top 10 cm profile (from 1986–1995 at 1° spatial resolution) to evaluate the terrestrial component of the land-atmosphere coupling strength. Furthermore, some recent studies (McColl, Wang, et al., 2017; McColl, Alemohammad, et al., 2017) report similar findings which highlight higher rates of SM drydowns in the arid and semi-arid climates.

4.3.3 Constant-rate losses (l_w and l_d)

Constant-rate loss of SM during the wet phase of the drydown is represented by l_w. This phase is characterized by abundant SM and hence, the land-atmospheric coupling is dominated by the availability of net radiation. Moisture-rich conditions also accentuates vegetation growth and may further add to high evapotranspiration losses to the atmosphere. Regions with notably high value of l_w correspond to CGS ecosystems and show a strong seasonal variability, which corresponds to the growth period of the vegetation in these ecosystems (**Figure** 9). High values of l_w can be seen in the pampas of South America, southwestern Africa and northeastern Australia during DJF and SON months. Croplands of U.S. Midwest, Sahel, Central Asia and India are seen to have high l_w values during MAM and JJA months. The pixel-scale l_w observed for CGS ecosystems at SMAP footprint can be the effective manifestation of several simultaneous drydown processes at the subgrid scale, with different drydown rates and dominant processes, as explained in section 4.2.3.

Constant-rate loss of SM during the dry phase is denoted by l_d. This phase is characterized by low SM and vegetation vigor and hence leading to diminished SM losses. Reduced soil moisture in this phase leads to diminished soil evaporation, higher sensible heat flux, and hence, enhanced boundary layer growth (Pan & Mahrt, 1987; Sanchez-Mejia & Papuga, 2014). Low values of l_d are observed for the arid ecosystems and deserts like Western and

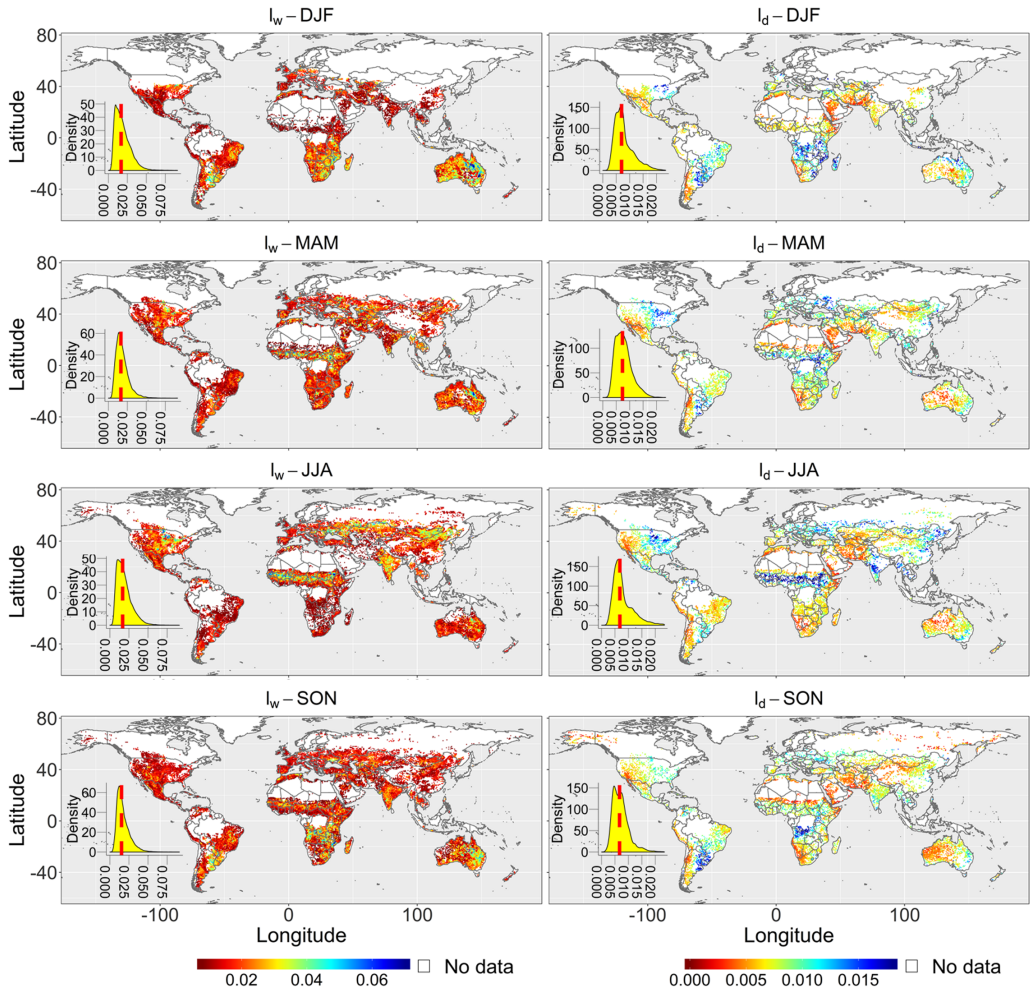

Figure 9. Same as Figure 6, for l_w and l_d (in $m^3/m^3/day$).

Central Australia, Kalahari Desert in southern Africa, Thar Desert in India, Atacama and Patagonian region in South America and parts of Central Asia and western U.S.

4.3.4 Inter-seasonal variability in drydown parameters

Figure 10 provides a comparison among seven governing parameters of $\boldsymbol{L(\theta_{RS})}$ summarized as boxplots for different climate, landcover and %clay classes. It is observed that the parameters θ^{TD}, m_1, m_2 and l_w show a high degree of variability compared to l_d, θ^{WT} and θ^{GW} across different landuse, climate and %clay classes. Among various landuse classes, the hi ghest inter-seasonal variability in the drydown parameters is observed in CGS landscapes due to significant changes in the land-surface characteristics across the seasons compared to arid shrublands and sparsely vegetated regions (Hirota et al., 2011; Whitley et al., 2017). Changes in the land-surface characteristics, high subgrid variability in precipitation and vegetation patterns in these ecosystems cause seasonal changes in the subgrid-scale variability of SM, leading to seasonal variability in land-atmospheric coupling, evaporation and transpiration, plant-water dynamics and vertical fluxes all factors which influence θ^{TD}, m_1, m_2 and l_w. Landcover characteristics can regulate drainage, ponding and thus impact infiltration, redistribution and evapotranspiration processes. In complex terrains with mixed vegetation, various vegetation-topography-soil combinations have been

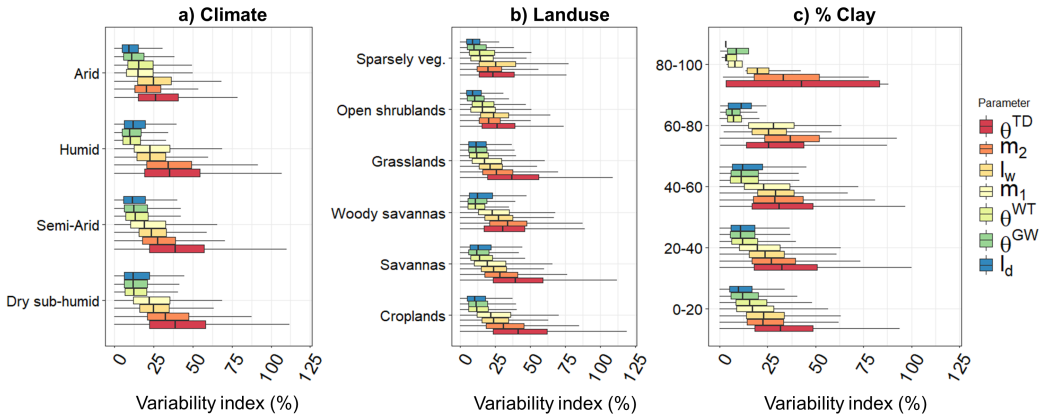

Figure 10. Comparison of the Variability Index (VI, in percentage) for drydown parameters summarized per *a*) climate, *b*) landuse and *c*) %clay classes.

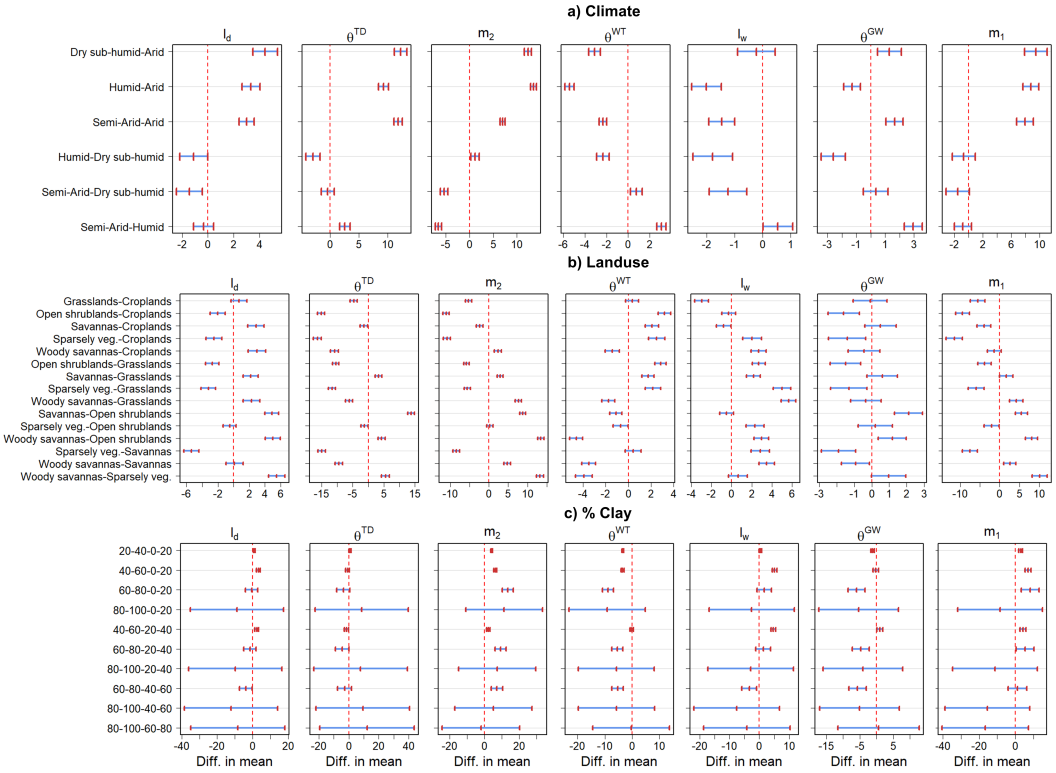

Figure 11. Pair-wise difference in the mean VI of the SM drydown parameters for different climate, landuse and %clay classes. The horizontal bars show the 95% confidence level for the class-wise difference in the mean VI of the respective parameters. The vertical red dashed line indicates no (zero) difference in the class-wise mean VI of the parameters. The difference in the mean is only statistically significant if the 95% confidence interval doesn't include zero (intersect the vertical line at difference in mean=0).

observed to influence the temporal persistence of SM patterns (Crow et al., 2012). Other drydown parameters namely, l_d, θ^{WT} and θ^{GW} relate to the extremes of the SM dynamics.

During very dry or wet conditions, the subgrid-scale variability in the SM is low (Gaur & Mohanty, 2016, 2019) and the control of SM on land-atmospheric interactions is limited. Hence, parameters l_d, θ^{WT} and θ^{GW} show low inter-seasonal variability. Furthermore, variability in the sensing depth of SMAP may change the support volume of the SMAP footprint over different seasons, adding significant variability in estimation of drydown parameters. While we assumes a uniform sensing depth of 5 cm for this study, several studies have reported a reduction in the sensing depth of microwave retrievals with an increase in the SM content (Escorihuela et al., 2010; Shellito et al., 2018). Strong inter-seasonal variability in the SMAP derived SM drydown parameters strengthen the argument in the favor of recognizing the temporal dimension in the SM drydown processes as hypothesized in this study.

We used Tukey's test (Bondar & Putter, 1968; Yandell, 1997) to evaluate the statistical significance of the difference in the inter-class (landuse, climate and %clay) means of VI for each SM drydown parameter (**Figure** 11). The results indicate that the difference in the mean VI of various SWRP_{eff} is statistically significant among climate and landuse classes as opposed to classification based on %clay. In other words, climate and landuse are observed to be better classifiers of the inter-seasonal variability in the SM drydown parameters compared to the %clay at the RS-footprint scale. These observations are supported by studies by Jana (2010), Crow et al. (2012) and Gaur and Mohanty (2016) which conceptualized that landcover patterns and meteorological forcings act as dominant controls of SM dynamics at RS-footprint scale.

4.4 Application and future work

4.4.1 Understanding land-atmospheric interactions and SM memory

The impact of SM on weather through evaporation and other surface energy fluxes is significant. The SM-atmospehric feedback has higher influence on precipitation than sea surface temperature anomalies, especially in the continental mid-latitudes during the summer months as seen in some atmospheric general circulation models (Koster, 2004). Quantification of the SM memory (m_2) and its inter-seasonal variability may have implications for improving seasonal to inter-annual climate predictions, particularly for summer forecasts for transition zones between dry and humid regions where models heavily depend on SM memory for simulations due to uncertainty in predicting precipitation (Dong et al., 2007; Koster et al., 2011; Koster & Suarez, 2001; Seneviratne et al., 2006).

4.4.2 Changes in SM retention under changing aridity and land use patterns

The study highlights that among other factors, the seasonal variability in the subgrid-scale variability in the land-surface characteristics have a significant impact on the SWRP_{eff} of the pixel. The land-surface characteristics and climate may moderate the net moisture retention by the soil at the RS-footprint scale. The present study may be expanded in future to quantify the changes in the global hydrological cycle because of modification in the SWRP_{eff} of soil across the globe under projected increase in global aridity, decrease in grassland coverage and change in landcover characteristics (Beck et al., 2018; Berg et al., 2016; Brookshire & Weaver, 2015; Hirota et al., 2011; Lickley & Solomon, 2018)

4.4.3 Transition between soil hydrologic regimes as drought indicator

Application of remotely sensed SM is demonstrated in several studies for large-scale drought monitoring (Martínez-Fernández et al., 2016; Mishra et al., 2017). These studies rely on pedotransfer function(s) and soil textural information to obtain soil wilting point and field capacity estimates for normalizing the SM observations as a drought index. We highlight that the SWRP_{eff} display high spatio-temporal variability across the globe. Hence,

use of seasonal and scale-specific, $SWRP_{eff}$ have potential to capture to subgrid-scale variability in the SM drydown patterns and may be applicable in monitoring the transition of soil from wet to dry hydrologic regimes. Use of the transition rate between dry and wet regime i.e. m_2 in a drought monitoring framework may help improve sensitivity to rapidly evolving "*flash-drought*" conditions.

4.4.4 Hydraulic parameterization of large-scale land-surface and earth-system models

SWRPs are important components of land-surface/ earth system models. However, most models depend on using some form of pedotransfer function to derive the estimates of the SWRPs for modeling (Gutmann & Small, 2007). These estimates are often used as calibration parameters to account for the subgrid-scale variability in the pixel, thus increasing the avenues of uncertainty and equifinality. The $SWRP_{eff}$ estimated in this study provide a scale-specific manifestation of the SM dynamics and may be tested in hydrological models for improved simulations. However, the use of empirical parameters will depend on the model parameterization and structure. The users are advised to regard the uncertainty in estimation of these parameters given the short-length of record (4 years) and retrieval issues in several parts of the world, prior to the application of the parameters to any existing modeling framework.

4.5 Limitations of the study

The study is limited by the accuracy and the length of observation period of SMAP. Shallow retrieval depth of 5 cm undermines the importance of the root zone SM dynamics, which is crucial for sustaining land-atmospheric interactions, vegetation growth, soil water storage, deep percolation and aquifer recharge etc. Long-term observations retrieved over the coming years of SMAP mission will reduce the uncertainty in the estimation of the parameters of $\boldsymbol{L(\theta_{RS})}$. High retrievals errors in complex terrains, heavily vegetated regions, snow-dominated areas and urban landscapes lead to large areas of flagged/ missed retrievals in ecologically important regions like Amazon, or snow-dominated regions like Alaska, and Canada and Northern U.S., most parts of Europe, especially during winter season. Furthermore, temporal revisit of 2-3 days negatively effects the ability of the proposed approach in identifying rapid processes in the SM drydown, especially the gravity-drainage phase. The study does not explicitly account for scenarios where the proposed monthly triplets (DJF, MAM, JJA, SON) may not be the best representation of the different features of the SM dynamics. For example, in the crop-dominated regions, SM dynamics might be better captured by explicitly accounting for the growing season, which might not necessarily follow the proposed monthly triplets used in this study. It is imperative to highlight that the parameters and interpretations of this study are scale-specific (36 km).

5 Conclusion

This study provides a global-scale parameterization of the seasonal surface SM drydowns using an unsupervised, data-driven methodology developed using retrievals from SMAP. A new non-parametric approach is developed to prescribe piecewise-linear canonical shapes of surface SM drydown for each SMAP pixel. This provides an independent validation of the SM drydown pathways suggested by several studies based on point-scale observations. Globally significant canonical shapes are then used to evaluate the best fitting curve on the seasonal values of $[-\Delta\theta_{RS}/\Delta t]$ v/s $[\theta_{RS}]$ using a non-linear least-squares approach.

Results indicate that a full drydown curve i.e. {FCFC} is rarely achieved, however several other combinations of the processes {FCF, CFC, C, F, CF and FC} are observed at

the RS scale, where "F" and "C" indicate falling-rate and constant-rate loss respectively. The effective SM drydown at RS footprint-scale is governed by a unique subset of the seven parameters comprising of the three SWRP_{eff} (θ^{GW}, θ^{WT}, θ^{TD}), the slope of falling-rate losses i.e. the gravity-drainage and transitional phase (m_1 and m_2) and the constant-rate loss during wet and dry phase (l_w and l_d), depending on the pathway of the drydown process. These parameters/processes of SM drydown are moderated by the effective manifestation of various soil, vegetation and atmospheric factors at the RS-footprint scale. The rate of loss of SM during the transition between wet and dry phase represents the terrestrial component of land-atmospheric coupling strength. High values of m_2 is observed for the arid and semi-arid regions, especially for the seasons when the atmospheric moisture demand is high. Seasonal variability in the meteorological drivers and land-surface characteristics yield a unique control over effective SM drydown for different landcovers and climate by moderating the subgrid-scale heterogeneity of the RS-footprint. This is manifested in strong inter-seasonal variability in the drydown parameters, especially, θ^{TD}, m_2 and l_w. Subgrid-scale heterogeneity in SM distribution leads to non-unique relationship between the effective drydown rate i.e. $[-\Delta\theta_{RS}/\Delta t]$ v/s $[\theta_{RS}]$, especially for croplands, grasslands and savanna ecosystems in the growing season. In the absence of the vegetative and atmospheric controls over SM dynamics in the dry conditions, the influence of soil texture on SM drydown becomes evident. Increase in the percentage of clay in soils increases the value of θ^{TD}, indicating soil-induced control on the effective wilting point of the pixel.

It is evident that the parameters of SM drydown patterns provide valuable insights about SM dynamics and its governing controls at large spatial scales. SM lies at the intersection of the global hydrological, carbon and energy cycles. Hence, the understanding of global-scale SM drydown processes (pathways and parameters), and seasonally varying governing controls will find diverse applications in the field of hydrology, soil physics and beyond.

Acknowledgments

The authors acknowledge the funding support from NASA SUSMAP project (NNX16AQ58G) titled, "Root Zone Soil Hydraulic Property Estimation by SMAP". We thank the Texas A&M High-Performance Research Computing (HPRC) for providing computing resource for the research. SMAP and Landcover SM data is available at NASA National Snow, and Ice Data Center Distributed Active Archive Center (NSIDC-DAAC): `http://nsidc.org/data/SPL3SMP`). Soil textural information is available at 0.05-degree spatial resolution from HWSD-v1.2 (`http://www.fao.org/soils-portal/soil-survey/soil-maps-and-databases/harmonized-world-soil-database-v12/en/`). The Aridity index is available at 30 arc-seconds (`https://www.cgiarcsi.community/data/global-aridity-and-pet-database/`). The dataset generated from this study is available at: Sehgal, V. (2019). Parameters of Global Surface Soil Moisture Drydown using SMAP, HydroShare, (`http://bit.ly/37jeVMq`). We are thankful to Dr. Ignacio Rodriguez-Iturbe, Texas A&M University and Dr. Dara Entekhabi, Massachusetts Institute of Technology for insightful discussion on improving the manuscript.

References

Akbar, R., Gianotti, D. J. S., McColl, K. A., Haghighi, E., Salvucci, G. D., & Entekhabi, D. (2018, may). Estimation of landscape soil water losses from satellite observations of soil moisture. *Journal of Hydrometeorology*, *19*(5), 871–889. Retrieved from `https://doi.org/10.1175%2Fjhm-d-17-0200.1` doi: 10.1175/jhm-d-17-0200.1

Ankenbauer, K. J., & Loheide, S. P. (2016, dec). The effects of soil organic matter on soil water retention and plant water use in a meadow of the sierra nevada, CA. *Hydrological Processes*, *31*(4), 891–901. Retrieved from `https://doi.org/10.1002%2Fhyp.11070` doi: 10.1002/hyp.11070

Arlot, S., & Celisse, A. (2010). A survey of cross-validation procedures for model selection. *Statistics Surveys*, *4*(0), 40–79. Retrieved from https://doi.org/10.1214%2F09-ss054 doi: 10.1214/09-ss054

Batjes, N. (2016, may). Harmonized soil property values for broad-scale modelling (WISE30sec) with estimates of global soil carbon stocks. *Geoderma*, *269*, 61–68. Retrieved from https://doi.org/10.1016%2Fj.geoderma.2016.01.034 doi: 10.1016/j.geoderma.2016.01.034

Baudena, M., DAndrea, F., & Provenzale, A. (2008, dec). A model for soil-vegetation-atmosphere interactions in water-limited ecosystems. *Water Resources Research*, *44*(12). Retrieved from https://doi.org/10.1029%2F2008wr007172 doi: 10.1029/2008wr007172

Beck, H. E., Zimmermann, N. E., McVicar, T. R., Vergopolan, N., Berg, A., & Wood, E. F. (2018, oct). Present and future köppen-geiger climate classification maps at 1-km resolution. *Scientific Data*, *5*(1). Retrieved from https://doi.org/10.1038%2Fsdata.2018.214 doi: 10.1038/sdata.2018.214

Belward, A. S., Estes, J. E., & Kline, K. D. (1999). The IGBP-DIS global 1-km land-cover data set DISCover: A project overview. *Photogrammetric Engineering and Remote Sensing*, *65*(9), 1013–1020. Retrieved from http://edcwww.cr.usgs.gov/landdaac/rKIWrkmhome-

Berg, A., Findell, K., Lintner, B., Giannini, A., Seneviratne, S. I., van den Hurk, B., ... Milly, P. C. D. (2016, may). Land–atmosphere feedbacks amplify aridity increase over land under global warming. *Nature Climate Change*, *6*(9), 869–874. Retrieved from https://doi.org/10.1038%2Fnclimate3029 doi: 10.1038/nclimate3029

Boivin, P. (2011). Shrinkage and swelling phenomena in soils. In *Encyclopedia of agrophysics* (pp. 733–735). Springer Netherlands. Retrieved from https://doi.org/10.1007%2F978-90-481-3585-1_139 doi: 10.1007/978-90-481-3585-1_139

Boivin, P., Garnier, P., & Tessier, D. (2004, jul). Relationship between clay content, clay type, and shrinkage properties of soil samples. *Soil Science Society of America Journal*, *68*(4), 1145–1153. Retrieved from https://doi.org/10.2136%2Fsssaj2004.1145 doi: 10.2136/sssaj2004.1145

Bonan, G. B., & Doney, S. C. (2018, feb). Climate, ecosystems, and planetary futures: The challenge to predict life in earth system models. *Science*, *359*(6375), eaam8328. Retrieved from https://doi.org/10.1126%2Fscience.aam8328 doi: 10.1126/science.aam8328

Bondar, J., & Putter, J. (1968, may). Simultaneous statistical inference. *Technometrics*, *10*(2), 415–416. Retrieved from https://doi.org/10.1080%2F00401706.1968.10490583 doi: 10.1080/00401706.1968.10490583

Brookshire, E. N. J., & Weaver, T. (2015, may). Long-term decline in grassland productivity driven by increasing dryness. *Nature Communications*, *6*(1). Retrieved from https://doi.org/10.1038%2Fncomms8148 doi: 10.1038/ncomms8148

Burgin, M. S., Colliander, A., Njoku, E. G., Chan, S. K., Cabot, F., Kerr, Y. H., ... Yueh, S. H. (2017, may). A comparative study of the SMAP passive soil moisture product with existing satellite-based soil moisture products. *IEEE Transactions on Geoscience and Remote Sensing*, *55*(5), 2959–2971. Retrieved from https://doi.org/10.1109%2Ftgrs.2017.2656859 doi: 10.1109/tgrs.2017.2656859

Chan, S., Bindlish, R., Hunt, R., Jackson, T., & Kimball, J. (2013). Soil moisture active passive (smap) ancillary data report: vegetation water content. *Pasadena, California*.

Colliander, A., Cosh, M. H., Misra, S., Jackson, T. J., Crow, W. T., Chan, S., ... Yueh, S. H. (2017, jul). Validation and scaling of soil moisture in a semi-arid environment: SMAP validation experiment 2015 (SMAPVEX15). *Remote Sensing of Environment*, *196*, 101–112. Retrieved from https://doi.org/10.1016%2Fj.rse.2017.04.022 doi: 10.1016/j.rse.2017.04.022

Crow, W. T., Berg, A. A., Cosh, M. H., Loew, A., Mohanty, B. P., Panciera, R., ... Walker, J. P. (2012, apr). Upscaling sparse ground-based soil moisture observations for the validation of coarse-resolution satellite soil moisture products. *Reviews of*

Geophysics, *50*(2). Retrieved from https://doi.org/10.1029%2F2011rg000372 doi: 10.1029/2011rg000372

Dirmeyer, P. A. (2011, aug). The terrestrial segment of soil moisture-climate coupling. *Geophysical Research Letters*, *38*(16), n/a–n/a. Retrieved from https://doi.org/10.1029%2F2011gl048268 doi: 10.1029/2011gl048268

D'Odorico, P., Ridolfi, L., Porporato, A., & Rodriguez-Iturbe, I. (2000, aug). Preferential states of seasonal soil moisture: The impact of climate fluctuations. *Water Resources Research*, *36*(8), 2209–2219. Retrieved from https://doi.org/10.1029%2F2000wr900103 doi: 10.1029/2000wr900103

Dong, J., Ni-Meister, W., & Houser, P. R. (2007, may). Impacts of vegetation and cold season processes on soil moisture and climate relationships over eurasia. *Journal of Geophysical Research*, *112*(D9). Retrieved from https://doi.org/10.1029%2F2006jd007774 doi: 10.1029/2006jd007774

Dunne, J. P., John, J. G., Adcroft, A. J., Griffies, S. M., Hallberg, R. W., Shevliakova, E., ... Zadeh, N. (2012, oct). GFDL's ESM2 global coupled climate–carbon earth system models. part i: Physical formulation and baseline simulation characteristics. *Journal of Climate*, *25*(19), 6646–6665. Retrieved from https://doi.org/10.1175%2Fjcli-d-11-00560.1 doi: 10.1175/jcli-d-11-00560.1

Escorihuela, M., Chanzy, A., Wigneron, J., & Kerr, Y. (2010, may). Effective soil moisture sampling depth of l-band radiometry: A case study. *Remote Sensing of Environment*, *114*(5), 995–1001. Retrieved from https://doi.org/10.1016%2Fj.rse.2009.12.011 doi: 10.1016/j.rse.2009.12.011

Fast, J. D., Berg, L. K., Feng, Z., Mei, F., Newsom, R., Sakaguchi, K., & Xiao, H. (2019, aug). The impact of variable land-atmosphere coupling on convective cloud populations observed during the 2016 HI-SCALE field campaign. *Journal of Advances in Modeling Earth Systems*, *11*(8), 2629–2654. Retrieved from https://doi.org/10.1029%2F2019ms001727 doi: 10.1029/2019ms001727

Fick, S. E., & Hijmans, R. J. (2017, may). WorldClim 2: new 1-km spatial resolution climate surfaces for global land areas. *International Journal of Climatology*, *37*(12), 4302–4315. Retrieved from https://doi.org/10.1002%2Fjoc.5086 doi: 10.1002/joc.5086

Flato, G. M. (2011, nov). Earth system models: an overview. *Wiley Interdisciplinary Reviews: Climate Change*, *2*(6), 783–800. Retrieved from https://doi.org/10.1002%2Fwcc.148 doi: 10.1002/wcc.148

Folberth, C., Skalský, R., Moltchanova, E., Balkovič, J., Azevedo, L. B., Obersteiner, M., & van der Velde, M. (2016, jun). Uncertainty in soil data can outweigh climate impact signals in global crop yield simulations. *Nature Communications*, *7*(1). Retrieved from https://doi.org/10.1038%2Fncomms11872 doi: 10.1038/ncomms11872

Gaur, N., & Mohanty, B. P. (2013, mar). Evolution of physical controls for soil moisture in humid and subhumid watersheds. *Water Resources Research*, *49*(3), 1244–1258. Retrieved from https://doi.org/10.1002%2Fwrcr.20069 doi: 10.1002/wrcr.20069

Gaur, N., & Mohanty, B. P. (2016, aug). Land-surface controls on near-surface soil moisture dynamics: Traversing remote sensing footprints. *Water Resources Research*, *52*(8), 6365–6385. Retrieved from https://doi.org/10.1002%2F2015wr018095 doi: 10.1002/2015wr018095

Gaur, N., & Mohanty, B. P. (2019, jan). A nomograph to incorporate geophysical heterogeneity in soil moisture downscaling. *Water Resources Research*, *55*(1), 34–54. Retrieved from https://doi.org/10.1029%2F2018wr023513 doi: 10.1029/2018wr023513

Guswa, A. J., Celia, M. A., & Rodriguez-Iturbe, I. (2002, sep). Models of soil moisture dynamics in ecohydrology: A comparative study. *Water Resources Research*, *38*(9), 5–1–5–15. Retrieved from https://doi.org/10.1029%2F2001wr000826 doi: 10.1029/2001wr000826

Gutmann, E. D., & Small, E. E. (2007, may). A comparison of land surface model soil hydraulic properties estimated by inverse modeling and pedotransfer functions. *Water Resources Research*, *43*(5). Retrieved from https://doi.org/10.1029%

2F2006wr005135 doi: 10.1029/2006wr005135

Haghighi, E., Gianotti, D. J. S., Akbar, R., Salvucci, G. D., & Entekhabi, D. (2018, mar). Soil and atmospheric controls on the land surface energy balance: A generalized framework for distinguishing moisture-limited and energy-limited evaporation regimes. *Water Resources Research*, *54*(3), 1831–1851. Retrieved from https://doi.org/10.1002%2F2017wr021729 doi: 10.1002/2017wr021729

Hillel, D. (2012). *Soil and water: physical principles and processes*. Elsevier.

Hirota, M., Holmgren, M., Nes, E. H. V., & Scheffer, M. (2011, oct). Global resilience of tropical forest and savanna to critical transitions. *Science*, *334*(6053), 232–235. Retrieved from https://doi.org/10.1126%2Fscience.1210657 doi: 10.1126/science.1210657

Hurrell, J. W., Holland, M. M., Gent, P. R., Ghan, S., Kay, J. E., Kushner, P. J., ... Marshall, S. (2013, sep). The community earth system model: A framework for collaborative research. *Bulletin of the American Meteorological Society*, *94*(9), 1339–1360. Retrieved from https://doi.org/10.1175%2Fbams-d-12-00121.1 doi: 10.1175/bams-d-12-00121.1

Ivanov, V. Y., Fatichi, S., Jenerette, G. D., Espeleta, J. F., Troch, P. A., & Huxman, T. E. (2010, sep). Hysteresis of soil moisture spatial heterogeneity and the "homogenizing" effect of vegetation. *Water Resources Research*, *46*(9). Retrieved from https://doi.org/10.1029%2F2009wr008611 doi: 10.1029/2009wr008611

Jackson, T., O'Neill, P., Chan, S., Bindlish, R., Colliander, A., Chen, F., & Dunbar, S. (2018). *Soil Moisture Active Passive (SMAP) Project: Calibration and Validation for the L2/3_SM_P Version 5 and L2/3_SM_P_E Version 2 Data Products Citation* (Tech. Rep.). Retrieved from https://pdms.jpl.nasa.gov/

Jana, R. (2010). *Scaling characteristics of soil hydraulic parameters at varying spatial resolutions*. Texas A&M University.

Kathuria, D., Mohanty, B. P., & Katzfuss, M. (2019, jan). A nonstationary geostatistical framework for soil moisture prediction in the presence of surface heterogeneity. *Water Resources Research*, *55*(1), 729–753. Retrieved from https://doi.org/10.1029%2F2018wr023505 doi: 10.1029/2018wr023505

Kirkham, M. (2005). Field capacity, wilting point, available water, and the non-limiting water range. In *Principles of soil and plant water relations* (pp. 101–115). Elsevier. Retrieved from https://doi.org/10.1016%2Fb978-012409751-3%2F50008-6 doi: 10.1016/b978-012409751-3/50008-6

Kohavi, R., et al. (1995). A study of cross-validation and bootstrap for accuracy estimation and model selection. In *Ijcai* (Vol. 14, pp. 1137–1145).

Kolassa, J., Reichle, R., Liu, Q., Alemohammad, S., Gentine, P., Aida, K., ... Walker, J. (2018, jan). Estimating surface soil moisture from SMAP observations using a neural network technique. *Remote Sensing of Environment*, *204*, 43–59. Retrieved from https://doi.org/10.1016%2Fj.rse.2017.10.045 doi: 10.1016/j.rse.2017.10.045

Koster, R. D. (2004, aug). Regions of strong coupling between soil moisture and precipitation. *Science*, *305*(5687), 1138–1140. Retrieved from https://doi.org/10.1126%2Fscience.1100217 doi: 10.1126/science.1100217

Koster, R. D., Mahanama, S. P. P., Yamada, T. J., Balsamo, G., Berg, A. A., Boisserie, M., ... Wood, E. F. (2011, oct). The second phase of the global land–atmosphere coupling experiment: Soil moisture contributions to subseasonal forecast skill. *Journal of Hydrometeorology*, *12*(5), 805–822. Retrieved from https://doi.org/10.1175%2F2011jhm1365.1 doi: 10.1175/2011jhm1365.1

Koster, R. D., & Suarez, M. J. (2001, dec). Soil moisture memory in climate models. *Journal of Hydrometeorology*, *2*(6), 558–570. Retrieved from https://doi.org/10.1175%2F1525-7541%282001%29002%3C0558%3Asmmicm%3E2.0.co%3B2 doi: 10.1175/1525-7541(2001)002⟨0558:smmicm⟩2.0.co;2

Laio, F., Porporato, A., Ridolfi, L., & Rodriguez-Iturbe, I. (2001, jul). Plants in water-controlled ecosystems: active role in hydrologic processes and response to water stress. *Advances in Water Resources*, *24*(7), 707–723. Retrieved from https://doi.org/

10.1016%2Fs0309-1708%2801%2900005-7 doi: 10.1016/s0309-1708(01)00005-7

Lickley, M., & Solomon, S. (2018, oct). Drivers, timing and some impacts of global aridity change. *Environmental Research Letters*, *13*(10), 104010. Retrieved from https://doi.org/10.1088%2F1748-9326%2Faae013 doi: 10.1088/1748-9326/aae013

Martínez-Fernández, J., González-Zamora, A., Sánchez, N., Gumuzzio, A., & Herrero-Jiménez, C. (2016, may). Satellite soil moisture for agricultural drought monitoring: Assessment of the SMOS derived soil water deficit index. *Remote Sensing of Environment*, *177*, 277–286. Retrieved from https://doi.org/10.1016%2Fj.rse.2016.02.064 doi: 10.1016/j.rse.2016.02.064

McColl, K. A., Alemohammad, S. H., Akbar, R., Konings, A. G., Yueh, S., & Entekhabi, D. (2017, jan). The global distribution and dynamics of surface soil moisture. *Nature Geoscience*, *10*(2), 100–104. Retrieved from https://doi.org/10.1038%2Fngeo2868 doi: 10.1038/ngeo2868

McColl, K. A., Wang, W., Peng, B., Akbar, R., Gianotti, D. J. S., Lu, H., ... Entekhabi, D. (2017, apr). Global characterization of surface soil moisture drydowns. *Geophysical Research Letters*, *44*(8), 3682–3690. Retrieved from https://doi.org/10.1002%2F2017gl072819 doi: 10.1002/2017gl072819

Mellinger, C. (2016). *Quantitative research methods in translation and interpreting studies*. Routledge. Retrieved from https://doi.org/10.4324%2F9781315647845 doi: 10.4324/9781315647845

Mishra, A., Vu, T., Veettil, A. V., & Entekhabi, D. (2017, sep). Drought monitoring with soil moisture active passive (SMAP) measurements. *Journal of Hydrology*, *552*, 620–632. Retrieved from https://doi.org/10.1016%2Fj.jhydrol.2017.07.033 doi: 10.1016/j.jhydrol.2017.07.033

Mohanty, B., & Skaggs, T. (2001, nov). Spatio-temporal evolution and time-stable characteristics of soil moisture within remote sensing footprints with varying soil, slope, and vegetation. *Advances in Water Resources*, *24*(9-10), 1051–1067. Retrieved from https://doi.org/10.1016%2Fs0309-1708%2801%2900034-3 doi: 10.1016/s0309-1708(01)00034-3

Mohanty, B., & Zhu, J. (2007, aug). Effective hydraulic parameters in horizontally and vertically heterogeneous soils for steady-state land–atmosphere interaction. *Journal of Hydrometeorology*, *8*(4), 715–729. Retrieved from https://doi.org/10.1175%2Fjhm606.1 doi: 10.1175/jhm606.1

Moré, J. J. (1978). The levenberg-marquardt algorithm: Implementation and theory. In *Lecture notes in mathematics* (pp. 105–116). Springer Berlin Heidelberg. Retrieved from https://doi.org/10.1007%2Fbfb0067700 doi: 10.1007/bfb0067700

Moustakas, A., Sakkos, K., Wiegand, K., Ward, D., Meyer, K. M., & Eisinger, D. (2009, dec). Are savannas patch-dynamic systems? a landscape model. *Ecological Modelling*, *220*(24), 3576–3588. Retrieved from https://doi.org/10.1016%2Fj.ecolmodel.2009.06.036 doi: 10.1016/j.ecolmodel.2009.06.036

Nachtergaele, F., Van Velthuizen, H., Verelst, L., Batjes, N., Dijkshoorn, K., Van Engelen, V., ... Shi, X. (2012). *Harmonized World Soil Database - Version 1.2* (Tech. Rep.). Retrieved from http://www.fao.org/3/aq361e/aq361e.pdf

ONeill, P., Entekhabi, D., Njoku, E., & Kellogg, K. (2010, jul). The NASA soil moisture active passive (SMAP) mission: Overview. In *2010 IEEE international geoscience and remote sensing symposium*. IEEE. Retrieved from https://doi.org/10.1109%2Figarss.2010.5652291 doi: 10.1109/igarss.2010.5652291

Pan, H.-L., & Mahrt, L. (1987, jan). Interaction between soil hydrology and boundary-layer development. *Boundary-Layer Meteorology*, *38*(1-2), 185–202. Retrieved from https://doi.org/10.1007%2Fbf00121563 doi: 10.1007/bf00121563

Pollard, D., & Radchenko, P. (2006, feb). Nonlinear least-squares estimation. *Journal of Multivariate Analysis*, *97*(2), 548–562. Retrieved from https://doi.org/10.1016%2Fj.jmva.2005.04.002 doi: 10.1016/j.jmva.2005.04.002

Rasch, D., Kubinger, K. D., & Moder, K. (2009, apr). The two-sample t test: pre-testing its assumptions does not pay off. *Statistical Papers*, *52*(1), 219–231. Retrieved from

https://doi.org/10.1007%2Fs00362-009-0224-x doi: 10.1007/s00362-009-0224-x

Reichle, R. H., De Lannoy, G. J., Liu, Q., Colliander, A., Conaty, A., Jackson, T., ... Koster, R. D. (2015). *Soil moisture active passive (smap) project assessment report for the beta-release l4_sm data product.* National Aeronautics and Space Administration, Goddard Space Flight Center.

Rodriguez-Iturbe, I. (2000, jan). Ecohydrology: A hydrologic perspective of climate-soil-vegetation dynamies. *Water Resources Research*, *36*(1), 3–9. Retrieved from https://doi.org/10.1029%2F1999wr900210 doi: 10.1029/1999wr900210

Rodriguez-Iturbe, I., Porporato, A., Ridolfi, L., Isham, V., & Coxi, D. R. (1999, oct). Probabilistic modelling of water balance at a point: the role of climate, soil and vegetation. *Proceedings of the Royal Society of London. Series A: Mathematical, Physical and Engineering Sciences*, *455*(1990), 3789–3805. Retrieved from https://doi.org/10.1098%2Frspa.1999.0477 doi: 10.1098/rspa.1999.0477

Sanchez-Mejia, Z. M., & Papuga, S. A. (2014, jan). Observations of a two-layer soil moisture influence on surface energy dynamics and planetary boundary layer characteristics in a semiarid shrubland. *Water Resources Research*, *50*(1), 306–317. Retrieved from https://doi.org/10.1002%2F2013wr014135 doi: 10.1002/2013wr014135

Santanello, J. A., Dirmeyer, P. A., Ferguson, C. R., Findell, K. L., Tawfik, A. B., Berg, A., ... Wulfmeyer, V. (2018, jun). Land–atmosphere interactions: The LoCo perspective. *Bulletin of the American Meteorological Society*, *99*(6), 1253–1272. Retrieved from https://doi.org/10.1175%2Fbams-d-17-0001.1 doi: 10.1175/bams-d-17-0001.1

Saxton, K. E., & Rawls, W. J. (2006, sep). Soil water characteristic estimates by texture and organic matter for hydrologic solutions. *Soil Science Society of America Journal*, *70*(5), 1569–1578. Retrieved from https://doi.org/10.2136%2Fsssaj2005.0117 doi: 10.2136/sssaj2005.0117

Schwingshackl, C., Hirschi, M., & Seneviratne, S. I. (2017, sep). Quantifying spatiotemporal variations of soil moisture control on surface energy balance and near-surface air temperature. *Journal of Climate*, *30*(18), 7105–7124. Retrieved from https://doi.org/10.1175%2Fjcli-d-16-0727.1 doi: 10.1175/jcli-d-16-0727.1

Schwingshackl, C., Hirschi, M., & Seneviratne, S. I. (2018, oct). A theoretical approach to assess soil moisture–climate coupling across CMIP5 and GLACE-CMIP5 experiments. *Earth System Dynamics*, *9*(4), 1217–1234. Retrieved from https://doi.org/10.5194%2Fesd-9-1217-2018 doi: 10.5194/esd-9-1217-2018

Seneviratne, S. I., Koster, R. D., Guo, Z., Dirmeyer, P. A., Kowalczyk, E., Lawrence, D., ... Verseghy, D. (2006, oct). Soil moisture memory in AGCM simulations: Analysis of global land–atmosphere coupling experiment (GLACE) data. *Journal of Hydrometeorology*, *7*(5), 1090–1112. Retrieved from https://doi.org/10.1175%2Fjhm533.1 doi: 10.1175/jhm533.1

Shellito, P. J., Small, E. E., & Livneh, B. (2018, mar). Controls on surface soil drying rates observed by SMAP and simulated by the noah land surface model. *Hydrology and Earth System Sciences*, *22*(3), 1649–1663. Retrieved from https://doi.org/10.5194%2Fhess-22-1649-2018 doi: 10.5194/hess-22-1649-2018

Small, R. J., Bacmeister, J., Bailey, D., Baker, A., Bishop, S., Bryan, F., ... Vertenstein, M. (2014, dec). A new synoptic scale resolving global climate simulation using the community earth system model. *Journal of Advances in Modeling Earth Systems*, *6*(4), 1065–1094. Retrieved from https://doi.org/10.1002%2F2014ms000363 doi: 10.1002/2014ms000363

Trabucco, A., & Zomer, R. (2019). Global Aridity Index and Potential Evapotranspiration (ET0) Climate Database v2. Retrieved from https://figshare.com/articles/Global{_}Aridity{_}Index{_}and{_}Potential{_}Evapotranspiration{_}ET0{_}Climate{_}Database{_}v2/7504448 doi: 10.6084/m9.figshare.7504448.v3

Troch, P. A., Carrillo, G., Sivapalan, M., Wagener, T., & Sawicz, K. (2013, jun). Climate-vegetation-soil interactions and long-term hydrologic partitioning: signatures of catchment co-evolution. *Hydrology and Earth System Sciences*, *17*(6), 2209–2217.

Retrieved from https://doi.org/10.5194%2Fhess-17-2209-2013 doi: 10.5194/hess-17-2209-2013

UNEP. (1997). *World atlas of desertification* (Tech. Rep.). London ;. 1997: United Nations Environment Programme. Retrieved from http://digitallibrary.un.org/record/245955

Viola, F., Daly, E., Vico, G., Cannarozzo, M., & Porporato, A. (2008, nov). Transient soil-moisture dynamics and climate change in mediterranean ecosystems. *Water Resources Research*, *44*(11). Retrieved from https://doi.org/10.1029%2F2007wr006371 doi: 10.1029/2007wr006371

Vivoni, E. R., Rodríguez, J. C., & Watts, C. J. (2010, feb). On the spatiotemporal variability of soil moisture and evapotranspiration in a mountainous basin within the north american monsoon region. *Water Resources Research*, *46*(2). Retrieved from https://doi.org/10.1029%2F2009wr008240 doi: 10.1029/2009wr008240

Walsh, R. P. D., & Lawler, D. M. (1981, jul). RAINFALL SEASONALITY: DESCRIPTION, SPATIAL PATTERNS AND CHANGE THROUGH TIME. *Weather*, *36*(7), 201–208. Retrieved from https://doi.org/10.1002%2Fj.1477-8696.1981.tb05400.x doi: 10.1002/j.1477-8696.1981.tb05400.x

Warkentin, B. P. (1962, feb). WATER RETENTION AND SWELLING PRESSURE OF CLAY SOILS. *Canadian Journal of Soil Science*, *42*(1), 189–196. Retrieved from https://doi.org/10.4141%2Fcjss62-024 doi: 10.4141/cjss62-024

Welch, B. L. (1947, jan). The generalization of students problem when several different population variances are involved. *Biometrika*, *34*(1/2), 28. Retrieved from https://doi.org/10.2307%2F2332510 doi: 10.2307/2332510

Whitley, R., Beringer, J., Hutley, L. B., Abramowitz, G., Kauwe, M. G. D., Evans, B., ... Yu, Q. (2017, oct). Challenges and opportunities in land surface modelling of savanna ecosystems. *Biogeosciences*, *14*(20), 4711–4732. Retrieved from https://doi.org/10.5194%2Fbg-14-4711-2017 doi: 10.5194/bg-14-4711-2017

Willmott, C. J., Robeson, S. M., & Matsuura, K. (2011, sep). A refined index of model performance. *International Journal of Climatology*, *32*(13), 2088–2094. Retrieved from https://doi.org/10.1002%2Fjoc.2419 doi: 10.1002/joc.2419

Yandell, B. S. (1997). Practical data analysis. In *Practical data analysis for designed experiments* (pp. 3–19). Springer US. Retrieved from https://doi.org/10.1007%2F978-1-4899-3035-4_1 doi: 10.1007/978-1-4899-3035-4_1

YUEN, K. K. (1974). The two-sample trimmed t for unequal population variances. *Biometrika*, *61*(1), 165–170. Retrieved from https://doi.org/10.1093%2Fbiomet%2F61.1.165 doi: 10.1093/biomet/61.1.165

Zscheischler, J., Orth, R., & Seneviratne, S. I. (2015, nov). A submonthly database for detecting changes in vegetation-atmosphere coupling. *Geophysical Research Letters*, *42*(22), 9816–9824. Retrieved from https://doi.org/10.1002%2F2015gl066563 doi: 10.1002/2015gl066563